Earth's Future

RESEARCH ARTICLE
10.1029/2023EF003734

Special Collection:
CMIP6: Trends, Interactions, Evaluation, and Impacts

Quantifying Contributions of External Forcing and Internal Variability to Arctic Warming During 1900–2021

Xiaodan Chen[1] and Aiguo Dai[2]

[1]Department of Atmospheric and Oceanic Sciences, Institute of Atmospheric Sciences, Fudan University, Shanghai, China, [2]Department of Atmospheric and Environmental Sciences, University at Albany, SUNY, Albany, NY, USA

Abstract Arctic warming has significant environmental and social impacts. Arctic long-term warming trend is modulated by decadal-to-multidecadal variations. Improved understanding of how different external forcings and internal variability affect Arctic surface air temperature (SAT) is crucial for explaining and predicting Arctic climate changes. We analyze multiple observational data sets and large ensembles of climate model simulations to quantify the contributions of specific external forcings and various modes of internal variability to Arctic SAT changes during 1900–2021. We find that the long-term trend and total variance in Arctic-mean SAT since 1900 are largely forced responses, including warming due to greenhouse gases and natural forcings and cooling due to anthropogenic aerosols. In contrast, internal variability dominates the early 20th century Arctic warming and mid-20th century Arctic cooling. Internal variability also explains ~40% of the recent Arctic warming from 1979 to 2021. Unforced changes in Arctic SAT are largely attributed to two leading modes. The first is pan-Arctic warming with stronger loading over the Eurasian sector, accounting for 70% of the unforced variance and closely related to the positive phase of the unforced Atlantic Multidecadal Oscillation (AMO). The second mode exhibits relatively weak warming averaged over the entire Arctic with warming over the North American-Pacific sector and cooling over the Atlantic sector, explaining 10% of the unforced variance and likely caused by the positive phase of the unforced Interdecadal Pacific Oscillation (IPO). The AMO-related changes dominate the unforced Arctic warming since 1979, while the IPO-related changes contribute to the decadal SAT changes over the North American-Pacific Arctic.

Plain Language Summary The Arctic warms much faster than the rest of the world, leading to significant local and remote influences. Warming in the Arctic is not uniform over time, with decadal-to-multidecadal variations upon the long-term trend. The changes in Arctic surface air temperature (SAT) can be attributed to either instrinct variability within the climate system or external forcings including anthropogenic factors such as greenhouse gases emission and natural factors such as volcanic eruptions. Understanding of the relative contributions of internal variability and external forcing to observed changes in Arctic SAT is crucial for improving Arctic climate projections in coming decades. By synthesizing multiple observational data sets and large-ensemble climate simulations, we find that the Arctic experienced long-term warming with some periods of slowdown in response to external forcing, which largely explains the overall change since 1900. Internal variability, particularly the multidecadal oscillation in the North Atlantic, dominates the early 20th century warming and mid-20th century cooling and significantly contributes to the recent rapid warming since 1979. A regression-based rescaling method removes systematic biases in model-simulated response (in comparison with observations), ensuring that our results are not influenced by the choice of climate models, as long as they are under the same historical forcing.

Key Points:

- Externally forced Arctic warming dominates the trend and variance in Arctic surface air temperature during 1900–2021
- Most of the internally generated Arctic temperature changes are related to the unforced Atlantic Multidecadal Oscillation
- Internal variability explains 40% of the Arctic warming from 1979 to 2021, while greenhouse gases and natural forcings account for the rest

Correspondence to:
X. Chen and A. Dai,
chenxd@fudan.edu.cn;
adai@albany.edu

Citation:
Chen, X., & Dai, A. (2024). Quantifying contributions of external forcing and internal variability to Arctic warming during 1900–2021. *Earth's Future*, *12*, e2023EF003734. https://doi.org/10.1029/2023EF003734

Received 19 APR 2023
Accepted 25 APR 2024

Author Contributions:
Conceptualization: Xiaodan Chen, Aiguo Dai
Formal analysis: Xiaodan Chen
Funding acquisition: Xiaodan Chen, Aiguo Dai
Investigation: Xiaodan Chen
Methodology: Aiguo Dai
Project administration: Xiaodan Chen
Software: Xiaodan Chen
Supervision: Aiguo Dai
Validation: Xiaodan Chen
Visualization: Xiaodan Chen
Writing – original draft: Xiaodan Chen
Writing – review & editing: Aiguo Dai

1. Introduction

Rapid Arctic warming is a robust feature of the ongoing climate change, with significant impacts on Arctic ecosystems and climate. Arctic warming rate is not homogeneous over time, with decadal-to-multidecadal variations that modulate the long-term warming trend (e.g., Bokuchava & Semenov, 2021; Chylek et al., 2014; England et al., 2021; Johannessen et al., 2004; Serreze & Barry, 2011; Serreze & Francis, 2006) and affect midlatitude climate (Dai & Deng, 2022; Wang & Chen, 2021). In general, the Arctic experienced accelerated warming in the early 20th century before the 1940s and in the recent decades since the 1980s, but between them the warming is relatively slow (e.g., Bokuchava & Semenov, 2021; England, 2021; Serreze & Barry, 2011; Svendsen et al., 2021). Climate model simulations exhibit a large spread in Arctic warming rate (Chylek et al., 2014; Ye & Messori, 2021), likely due to models' different climate sensitivity to historical forcings and their

different realizations of internal variability. Reducing the large spread in Arctic climate projections requires improved quantitative understanding of the relative roles of external forcing and internal variability in observed changes of Arctic surface air temperature (SAT).

Atmospheric circulation anomalies around the Arctic have been considered as a major cause of the accelerated Arctic warming and sea-ice loss in the recent decades (Ding et al., 2017; Francis & Wu, 2020; Kwok et al., 2013; Liu et al., 2021; Polyakov & Johnson, 2000; Zhang et al., 2008). Changes in stationary waves (e.g., Sang et al., 2021), atmospheric blockings (e.g., Chen et al., 2018), and cyclones moving into the Arctic (e.g., Sorteberg & Kvingedal, 2006) are also suggested to have contributed to observed multidecadal variations in Arctic SAT. However, as the atmosphere circulation itself has a short memory of 1–2 weeks, its decadal-to-multidecadal variations are likely induced by external forcing or internal variability originated below the atmosphere.

The atmospheric circulation anomalies associated with Arctic warming have been attributed to sea surface temperature (SST) changes in the tropical Pacific (e.g., Baxter et al., 2019; Clark & Lee, 2019; Ding et al., 2014, 2019; Sun et al., 2019). Some studies suggested that cold SST anomalies or SST cooling trends in the equatorial central-eastern Pacific (ECEP) can suppress tropical convection and generate upper-level divergence anomalies in the subtropics, resulting in a wave-train structure with a high-pressure center around Greenland, which leads to adiabatic warming centered in Greenland and spreading across the whole Arctic (e.g., Baxter et al., 2019; Ding et al., 2014, 2019). According to Ding et al. (2017), this wave-train structure associated with the ECEP cooling has strengthened since 1979, which is largely due to internal variability. The extratropical Pacific may also have an impact on Arctic SAT. Using partially coupled model simulations, Svendsen et al. (2018, 2021) found comparable effects of the tropical and extratropical Pacific on the multidecadal variations of Arctic SAT. They suggested that half of the early 20th century Arctic warming from 1915 to 1940 is attributable to a negative-to-positive phase transition of the Interdecadal Pacific Oscillation (IPO) that intensifies the Aleutian Low and the associated warm advection into the Arctic (primarily over the Pacific sector). This IPO phase transition can also result in adiabatic heating from subsidence (over the pan Arctic) by strengthening upward propagating waves over the North Pacific and thus weakening the polar vortex (Svendsen et al., 2018). Furthermore, based on atmospheric model simulations with prescribed SST, the IPO's positive phase plays a crucial role in the early 20th century Arctic warming, with its tropical component more related to the North American Arctic warming and its extratropical component more related to the Eurasian Arctic warming (Tokinaga et al., 2017). A positive IPO has a warm center in the ECEP, which is opposite to the cold ECEP-warm Arctic relationship after 1979 established by many studies (e.g., Ding et al., 2014, 2019). Moreover, from the 1990s to the 2000s, IPO's phase changed from positive to negative (Hua et al., 2018), yet Arctic warming accelerated during this period when the externally forced global warming rate did not accelerate (Dai et al., 2015). Thus, there exist a major inconsistency regarding the relationship between decadal-to-multidecadal variations in the Pacific SST and Arctic SAT.

On the other hand, it is widely agreed that Arctic warming can be induced by a positive or warm phase of the Atlantic Multidecadal Oscillation (AMO; e.g., Beitsch et al., 2014; Chylek et al., 2009; Johannessen et al., 2004; Tokinaga et al., 2017). Positive AMO can warm the Arctic and melt sea ice either by anomalous ocean heat transport into the Norwegian Sea, Barents and Kara Seas (e.g., Auclair & Tremblay, 2018; Beitsch et al., 2014; Bengtsson et al., 2004; Goosse & Holland, 2005; Jungclaus & Koenigk, 2010) or via atmospheric circulation responses to AMO-related SST anomalies (e.g., Castruccio et al., 2019). Once oceanic heat transport triggers decadal-to-multidecadal anomalies in Arctic SST and sea ice, sea ice-atmosphere interactions can significantly amplify the signal in the Arctic and subpolar regions, which in turn amplifies the AMO in the Atlantic (Deng & Dai, 2022). Despite considerable efforts devoted into understanding how IPO and AMO affect the decadal-to-multidecadal variations in Arctic SAT, their relative contributions have not been fully quantified or understood. Furthermore, the recent AMO and IPO cycles are not completely internally generated as they are significantly influenced by decadal variations in external forcing (Hua et al., 2018; Qin et al., 2020a), which further obscures their relationship with Arctic SAT variations, as the external forcing can simultaneously affect the Arctic without invoking the AMO- or IPO-like SST anomalies.

Besides the influence of oceanic low-frequency variability, nonlinear external forcing may also contribute to decadal-to-multidecadal variations in Arctic SAT. The ensemble mean of the all-forcing simulations by many climate models exhibits decadal-to-multidecadal variations superimposed on the overall warming trend in Arctic SAT (e.g., Beitsch et al., 2014; England, 2021), clearly indicating a nonlinear component of the forced changes. However, the relative contributions of various external forcings to the observed decadal-to-multidecadal

fluctuations in Arctic SAT depend on the models used in the estimate. Among 18 models participated in the Coupled Model Intercomparison Project phase 5 (CMIP5), the six models with individual simulations most similar to the observation can reproduce the observed Arctic cooling from 1939 to 1970 while the six most dissimilar models show no Arctic cooling trend at all during this period (Fyfe et al., 2013). In fact, matching individual model runs with observations should not be used to measure model performance in simulating Arctic SAT changes because the internal variations in observations and individual runs can be different. Moreover, as models' climate sensitivity and hence the simulated response may differ from reality, the ensemble mean of historical model simulations should not be used directly as the forced component in observed Arctic SAT, as done previously (e.g., Bokuchava & Semenov, 2021; England, 2021; Johannessen et al., 2004). Instead, rescaling of the model-simulated response should be used to remove any systematic mean biases in the simulated response to historical forcing, as done in this study.

Due to these difficulties, quantifying the relative contributions of internal variability and various external forcings to observed Arctic SAT changes remains challenging. In this study, we derive a more realistic and robust forced signal from a 100-member Community Earth System Model version 2 (CESM2) Large Ensemble (CESM2LE) (Rodgers et al., 2021) under the more accurate radiative forcing used in the Coupled Model Intercomparison Project phase 6 (CMIP6, Eyring et al., 2016). We extract the externally forced (EX) component of Arctic SAT changes through a rescaling method that accounts for the mean bias in models' climate sensitivity or forcing. Using CESM2 single-forcing runs, we further attribute the forced Arctic SAT changes to specific forcings. We also analyze the leading modes of internally generated (IV) Arctic SAT changes, which is the residual in the observed SAT anomalies after removing the EX component, and their relationships with decadal-to-multidecadal SST variations in the North Atlantic and Pacific Oceans. Furthermore, we analyzed Arctic response to observed SST anomalies associated with AMO or IPO in a coupled model (pacemaker runs) to quantify the impacts on Arctic SAT from AMO or IPO. Our results should improve current understanding of how individual external forcings and variability inherent in the North Atlantic and Pacific Oceans contribute to the observed Arctic warming. These findings have important implications for constraining the uncertainty in future Arctic projections.

2. Data and Methods

2.1. Observations

Three observational global data sets for monthly SAT are used in this study: GISTEMP4 from NASA GISS on $2° \times 2°$ grids (Lenssen et al., 2019), HadCRUT5 from CRU/Hadley Centre on $5° \times 5°$ grids (Morice et al., 2020), and Berkeley Earth Surface Temperature (BEST) on $1° \times 1°$ grids (Rohde et al., 2013). GISTEMP4 and HadCRUT5 are combined data sets derived by blending SAT observations from weather stations over land with SST observations from ships, buoys, and other sensors. BEST has two versions with different data over the sea-ice covered areas: one uses inferred SAT calculated from weather station SAT records through statistical methods and the other uses SST observations. The first one is used here. We focus on the 1900–2021 period with relatively homogeneous and abundant observations. Observational monthly SST on $1° \times 1°$ grids over 1900–2021 from Hadley Center Sea Ice and Sea Surface Temperature data set (HadISST, Rayner et al., 2003) is used. HadISST calculates SST near sea-ice edge using statistical relationships between SST and sea ice concentration and assigns a fixed value for the areas with sea ice cover greater than 90%. The monthly data of sea level pressure (SLP), geopotential height, horizontal winds, and precipitation are obtained from ERA5 (for 1950–2021, Hersbach et al., 2020) and ERA-20C (for 1900–1949, Poli et al., 2016) reanalysis data sets. We rescaled the ERA-20C anomaly using the ratio of standard deviations over 1950–2020 between ERA5 and ERA-20C to reduce the inhomogeneity in their variance. The anomalies from ERA5 and ERA-20C are relative to their own monthly climatology over a common period from 1979 to 2010.

2.2. Large-Ensemble Simulations

We estimated the forced signal mainly using CESM2LE, which has 100 ensemble runs under CMIP6 historical forcing from 1900 to 2014 and SSP3-7.0 emissions scenario from 2015 to 2100 (Rodgers et al., 2021). These members have random and different internal atmospheric and oceanic variability but the same external forcing, despite small differences in biomass burning representation. Twenty of them began from 20 different years from a PI (pre-industrial) control simulation with various Atlantic meridional overturning circulation (AMOC) states, while the remaining 80 runs begun from four selected years from the PI control run corresponding to the

maximum, decreasing, minimum, and increasing state of the AMOC (20 runs for each start year), with micro-perturbations in atmospheric temperature. The ensemble mean of CESM2LE represents primarily the response to external forcing with very small contributions from internal variability, especially for regional averages such as Arctic-mean SAT. Below, we will demonstrate that the variance of internal variability (e.g., IPO) in individual runs has been significantly reduced in the ensemble mean. The CESM2 exhibits significant improvements from its order generations, Community Earth System Model v1 Large Ensemble (CESM1LE), in the representation of Northern Hemisphere atmospheric circulations (such as storm tracks, stationary waves, atmospheric blocking) and has good performance compared to other CMIP6 models (Simpson et al., 2020).

Unlike the CESM2LE, the CESM1LE simulations uses CMIP5 historical (up to 2005) and RCP8.5 (2006 onwards) radiative forcing and initialized from the same ocean and sea ice conditions and micro perturbations in atmospheric temperature (Kay et al., 2015). While CESM1 better match the observed magnitude of Arctic Amplification than CESM2 (Chylek et al., 2023), the temporal evolution of external forcing in CMIP6 simulations is more realistic than that in CMIP5 simulations, particularly after 2005. As we will explain in Section 2.3, accurate temporal evolution of external forcing is crucial for determining the EX component in observations. Because of our use of the regression-based rescaling (also see Section 2.3) in estimating the forced component in observed SAT, the mean warming biases of the CESM2LE revealed by Chylek et al. (2023) should not affect our results, as we show below.

The CESM2LE and CESM1LE differ both in the model structure and forcing. In order to understand the different results estimated using CESM2LE and CESM1LE, we further analyzed a CESM2-CMIP5 forcing ensemble, which includes 10 ensemble runs by the CESM2 with CMIP5 historical and RCP8.5 forcing as in CESM1LE, so that the difference between CESM1LE and CESM2-CMIP5 forcing represents the impact of the model changes.

Large ensemble simulations from three other CMIP6 models are also analyzed: ACCESS-ESM1-5, MPI-ESM1-2-LR, and MIROC6. The first two use the same radiative forcing as CESM2LE and have 40 and 30 runs, respectively. The last one has 33 runs for the historical and SSP2-4.5 forcing scenarios. Responses to SSP3-7.0 and SSP2-4.5 forcings are very similar up to the middle 21st century (Davy & Outten, 2020). Although CMIP5 offer more large ensembles than CMIP6 and they have been widely used to study Arctic changes (e.g., Baxter et al., 2019; England et al., 2021; Pauling et al., 2021), CMIP6 models apply more accurate forcing from 2005 to 2015 and exhibit significant improvements in the simulation of Arctic sea ice and near surface temperatures (Davy & Outten, 2020).

To isolate the effects of individual external forcings, we further analyzed four CESM2 single-forcing ensembles in which only the interested forcing evolves with time while other forcings are fixed at the PI values. Three of them used individual forcings that are the same as CESM2LE: greenhouse gas (GHG), anthropogenic aerosols (AA), and biomass burning aerosols (BBA), respectively; while the other one used the else external forcings (EE; mainly including the natural radiative forcing, e.g., solar insolation and stratospheric volcanic aerosols). BBA includes the aerosols due to human biomass burning for agricultural, land use and fuels, as well as natural wildfires. AA includes industrial, agricultural, domestic and transport-related aerosol emissions, excluding BBA. These single-forcing ensembles used the same model and individual forcings as CESM2LE; therefore, they can be used to analyze the respective effects of the individual external forcings.

To examine the relationship between unforced Arctic SAT and decadal-to-multidecadal variations in the North Atlantic and Pacific Oceans, we utilized two sets of idealized pacemaker experiments using Community Earth System Model version 1 (CESM1; Hurrell et al., 2013), the predecessor of CESM2. One set has two thirty-member ensembles restoring idealized positive and negative AMO patterns over 8°N–65°N Atlantic (i.e., idealized AMO^+ and AMO^- pacemaker experiments; Castruccio et al., 2019); the other set has two ten-member ensembles restoring idealized positive and negative IPO patterns over 40°S–60°N Pacific (i.e., idealized IPO^+ and IPO^- pacemaker experiments; Meehl et al., 2021); the rest of the model is fully coupled. Radiative forcing is fixed at the PI level to eliminate the influence of external forcing. The ensemble members for each experiment are initialized with small atmospheric temperature perturbations. Each simulation runs for a decade. The idealized AMO and IPO configurations are obtained by regressing unforced SST series at each grid point onto the AMO and IPO indices defined by NCAR (Meehl et al., 2021). The unforced SST series are estimated as the residuals of observed SST series after subtracting the forced SST series derived from CMIP5 multimodel ensemble simulations using a signal-to-noise maximizing empirical orthogonal function (EOF) method (Ting et al., 2009).

2.3. Methods

Following previous studies (e.g., Dai et al., 2015; Qin et al., 2020a, 2020b), we used the ensemble-mean annual-mean anomaly timeseries (x) averaged over the Arctic (67°–90°N) from an all-forcing or a single-forcing ensemble to approximately represent the forced signal over the Arctic. The anomalies are relative to the 1901–1970 mean. We then obtained the EX component (Y_{EX}) in observations at each grid point (y, with mean removed) by scaling x with the regression coefficient (b) between x and y over 1900–2021: $Y_{EX} = bx$. The scaling by b is to account for any systematic bias in model-simulated long-term response to external forcing or biases in external forcings, and it greatly reduces the sensitivity of the estimated EX component to model mean biases as shown below. The use of the long period from 1900 to 2021 in the regression ensures that internal decadal-multidecadal variations would not be aliased with the forced long-term change (x). We found that b is around 0.75 in the Arctic between the observed and CESM2LE SAT, suggesting that CESM2 slightly overestimates the forced response to historical forcing (either due to errors in its climate sensitivity or historical forcing data). The values of b for the other three CMIP6 models (ACCESS-ESM1-5, MPI-ESM1-2-LR, and MIROC6) range from 0.85 to 1.10. This implies that if we were to directly use the ensemble-mean SAT to estimate the EX component without rescaling, as has been done previously (e.g., Fyfe et al., 2021; Suo et al., 2013), the estimates would vary considerably among the models.

When using an all-forcing large ensemble to derive Y_{EX}, the residual in y (i.e., $y - bx$) represents mainly the local unforced internally generated (IV) component. As such, we decomposed the total variations and changes in observations into the EX and IV components over the period from 1900 to 2021 at each grid point. Using CESM2LE ensemble-mean local anomaly at each grid point or global-mean anomaly as the forced signal does not alter the results greatly (not shown). When using a single-forcing large ensemble to derive the Y_{EX}, we can obtain the EX component due to the specific forcing. We then applied a 10-year low-pass Butterworth filtering on the EX and IV timeseries to focus on decadal-to-multidecadal variations and long-term changes. Area-weighting was used in regional averaging. A bootstrap algorithm was used to test the significance of correlation between two low-pass filtered timeseries, which requires no assumptions about distributions or autocorrelations. We reordered the timeseries randomly and calculated the correlation coefficient between them. Repeating the process 10,000 times allows us to construct a correlation distribution. A correlation coefficient that falls below the 2.5th or above the 97.5th percentile of the bootstrapped distribution is statistically significant at the 5% level based on a two-tailed test.

The AMO index is defined as the linearly detrended, 10-year low-pass filtered SST anomaly timeseries averaged over the North Atlantic (80°W–0°, 0°N–60°N, outlined in Figures 6a–6c), following Qin et al. (2020b). The IPO index is calculated using $SST_2 - (SST_1 + SST_3)/2$ (Henley et al., 2015), where SST_1, SST_2, and SST_3 are 10-year low-pass filtered SST anomaly timeseries averaged over three regions respectively: the northwestern Pacific (NWP, 140°E–145W°, 25°N–45°N), ECEP (170°E–90W°, 10°S–10°N), and southwestern Pacific (SWP, 150°E–160W°, 50°S–15°S), which are outlined in Figures 6d–6f. Using linear regression between CESM2LE ensemble-mean global-mean SST anomalies (x) and observed SST anomalies at each grid point (y) over 1900–2021, the EX and IV components of the observed SST anomalies are obtained, from which we calculate the IV components of the AMO and IPO indices. The IV components of the AMO and IPO indices in the individual runs are calculated by subtracting the ensemble-mean of the AMO and IPO indices from individual runs. After removing the ensemble mean, both the IV AMO and IPO indices are uncorrelated [$r = -0.008 \pm 0.124$ (mean $\pm$ std) for IV AMO and $r = -0.008 \pm 0.116$ for IV IPO] among the CESM2LE runs. According to our estimates below, the Arctic SAT changes related to the IV components of AMO and IPO are independent to the EX component of the observed Arctic SAT ($r = 0.09$ and -0.07, respectively). Despite the different approaches for obtaining the unforced SST series, the SST anomalies associated with the IV component of AMO (IPO) are similar to the SST differences between idealized AMO^+ and AMO^- (IPO^+ and IPO^-) pacemaker simulations (shown below).

The IPO variance in individual runs has been greatly reduced to approximately 1% in the CESM2LE ensemble mean IPO index, which is uncorrelated with Arctic-mean SAT. As a result, the externally forced SAT signal in the Arctic, which is derived from the ensemble mean, should not include influence from internal IPO. This also supports that the ensemble mean can be considered the forced signal. However, the ensemble-mean AMO index does show substantial multidecadal variations, primarily representing the impact of anthropogenic and volcanic aerosols (e.g., Booth et al., 2012; Mann & Emanuel, 2006; Murphy et al., 2017; Qin et al., 2020a; Watanabe & Tatebe, 2019). Thus, the impact of ensemble-mean AMO on Arctic SAT may be obscured by the non-direct

impact from the simultaneous external forcing. This is beyond the scope of this study. Our primary focus here is on the relationship between the IV components in the Arctic, Pacific, and North Atlantic.

3. Results

3.1. Forced and Unforced SAT Changes and the Roles of Various External Forcings

The observed Arctic-mean SAT anomaly series (Figure 1a) are similar among the three data sets, showing rapid warming from 1917 to 1938, steady cooling from 1938 to 1965, mild warming from 1965 to 1987, and accelerated warming since 1987. Figure 1b shows the EX and IV components in observed SAT estimated through linear regression using CESM2LE ensemble-mean Arctic-mean SAT anomaly timeseries as the forced signal. The three observational data sets produce nearly identical EX components ($r > 0.99$; dashed lines in Figure 1b) that represent a long-term warming trend with some slowdown from the 1940s–1960s and a pause in the early 1990s after the Pinatubo eruption.

In contrast, the estimated IV components differ noticeably among the three data sets (solid lines in Figure 1b); nevertheless, they all show decadal cooling from around 1904–1917, warming from 1917 to 1938, cooling from 1938 to 1965, and warming since about 1987. The IV and EX components of the observed Arctic SAT are unrelated ($r = 0.01$; Figure 1b), suggesting that the influences of the internal variability and external forcings are largely independent. As shown in Figure 1c, these IV-induced decadal trends contribute greatly to the decadal variations in the warming rates of Arctic SAT seen in observations, especially during the early 20th century warming from 1917 to 1938 (~67%) and mid-20th century cooling 1938–1965 (~104%). While the unforced component exhibits no significant long-term trends from 1900 to 2021 (Figure 1c) and only accounts for ~20% of the overall variance since 1900 (Figure 1b), it accounts for ~40% of the rapid warming since 1979 (Figure 1c). As BEST employs more station observations and advanced algorithms to estimate the SAT over the sea-ice covered area and has a higher a horizontal resolution compared to the other two data sets, the following results regarding the estimated EX and IV components of SAT (shown in Figures 2b, 2c, 3b, 4b–4i, 5, 10, 11, and 12) are based on BEST. Using the other two observational SAT data sets did not significantly alter the overall results, except for a minor overestimate (underestimate) of the contribution from the estimated IV component to the early 20th century warming (rapid Arctic warming in recent three decades).

The forced signals for Arctic SAT from the CESM2LE and three CMIP6 large ensembles, which are defined as ensemble-mean Arctic-mean SAT anomalies in individual models, differ substantially after 1960 (Figure 2a, partly due to the use of 1901–1970 as the reference period). The CESM2LE has forced signal time series in the upper range among the four CMIP6 ensembles (Figure 2a). This is likely due to its enhanced cloud feedback and high equilibrium climate sensitivity (Danabasoglu et al., 2020; Meehl et al., 2020). However, the EX components in observed SAT estimated using these forced signals and the rescaling method are very similar ($r > 0.99$; red lines in Figure 2b). Using the forced signals (white bars in Figure 2c) directly without the rescaling would overestimate the contributions from external forcing to the observed Arctic SAT trends by ~10% over the selected periods and lead to larger uncertainties. This indicates that the rescaling method can effectively eliminate the effect of the model biases in the simulated response to historical external forcing, making the estimated EX components in observations insensitive to the model mean biases in simulating the forced response. Thus, the rescaling method avoids the difficulty in choosing the forced response from a certain model.

Using the forced signal derived from a 40-member CESM1 Large Ensemble (CESM1LE) (Kay et al., 2015) did not significantly change our estimates of EX and IV components (solid and dotted lines in Figure 3b). The correlation coefficient between the EX (IV) components estimated using CESM2LE and CESM1LE reaches 0.97 (0.94), with $p < 0.01$. However, there is a notable difference after 2000: the EX component estimated using CESM1LE shows a quasi-linear warming trend after 2000, whereas that estimated using CESM2LE reveals a weakened warming trend from the 2000s to the 2010s. The difference is strongly related to the discrepancy in their forced signals (Figure 3a). The similarity of EX components estimated using CESM1LE and a 10-member CESM2 ensemble forced by CMIP5 forcing (CESM2LE-CMIP5 forcing; dash-and-dot line in Figure 3b) suggests that this difference is due to the use of CMIP5 forcing in CESM1LE, rather than the model differences. As a result, the contribution of external forcing to the observed warming trend estimated using CESM2LE gradually weakens from 1987 to 2016; in contrast, the contribution estimated using CESM1LE remains nearly consistent during this period. Nevertheless, the warming trends due to external forcing estimated using CESM1LE and CESM2LE are similar as long as we do not focus on short periods after 2000.

10.1029/2023EF003734

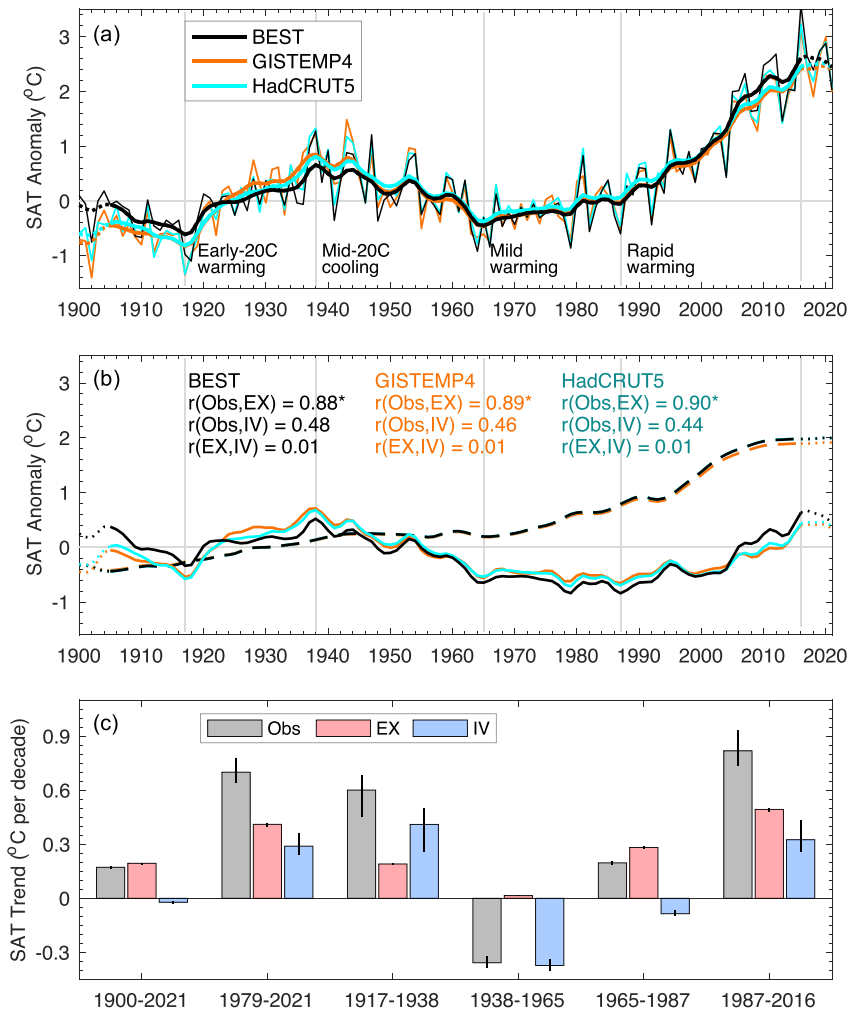

Figure 1. Observed, forced, and unforced Arctic surface air temperature (SAT) anomalies (°C, relative to 1901–1970 mean). (a) Annual (thin lines) and 10-year low-pass filtered (thick lines) SAT anomalies averaged over the Arctic (67°–90°N) from 1900 to 2021 in Berkeley Earth Surface Temperature (black lines), GISTEMP4 (orange lines), and HadCRUT5 (cyan lines) data sets, and (b) low-pass filtered time series of their externally forced (EX, dashed lines) and internally generated (IV, solid lines) components estimated through linear regression using CESM2LE ensemble-mean Arctic-mean SAT time series as the forced signal. Dotted lines are used for the beginning and ending 5 years of low-pass filtered time series since they are based on mirrored data and thus are less reliable. The correlation coefficients (r) between observed, EX, and IV time series are shown in (b), with a superscript star indicating statistical significance at the 5% level. (c) Linear trends (°C per decade) of the low-pass filtered time series of observed Arctic-mean SAT (gray bars) and its EX (red bars) and IV components (blue bars) over 1900–2021, 1979–2021, and four selected periods (shown in a and b) averaged across the three observational data sets, with their spreads shown by vertical lines.

The forced signals for Arctic SAT in the CESM2 single-forcing ensembles can generally sum up to the overall forced signal in CESM2LE, but with slower warming rates after 1990 (Figure 4a). It is likely due to that the increasing surface albedo and cooling surface temperature in the AA simulations result in a positive feedback of cooling through increasing sea ice and snow (Deng et al., 2020), while this positive feedback does not exist in reality nor in CESM2LE because of the overwhelming warming effect from GHGs. The artificial cooling in the AA ensemble mean can be reduced using the rescaling method (blue lines in Figures 4a and 4b). The linear combination of the EX components estimated using the forced signals in four single-forcing ensembles and the rescaling method generally replicates the temporal variations of the EX component estimated using the forced signal in CESM2LE (dotted and solid black lines in Figure 4b; $r = 0.97$) and the trend pattern over the Arctic from 1900 to 2021 (Figures 4h and 4i; pattern correlation coefficient $r = 0.96$), while the linear combination shows larger decadal variations and regional trend differences likely due to the nonlinear response (Deng et al., 2020) or

10.1029/2023EF003734

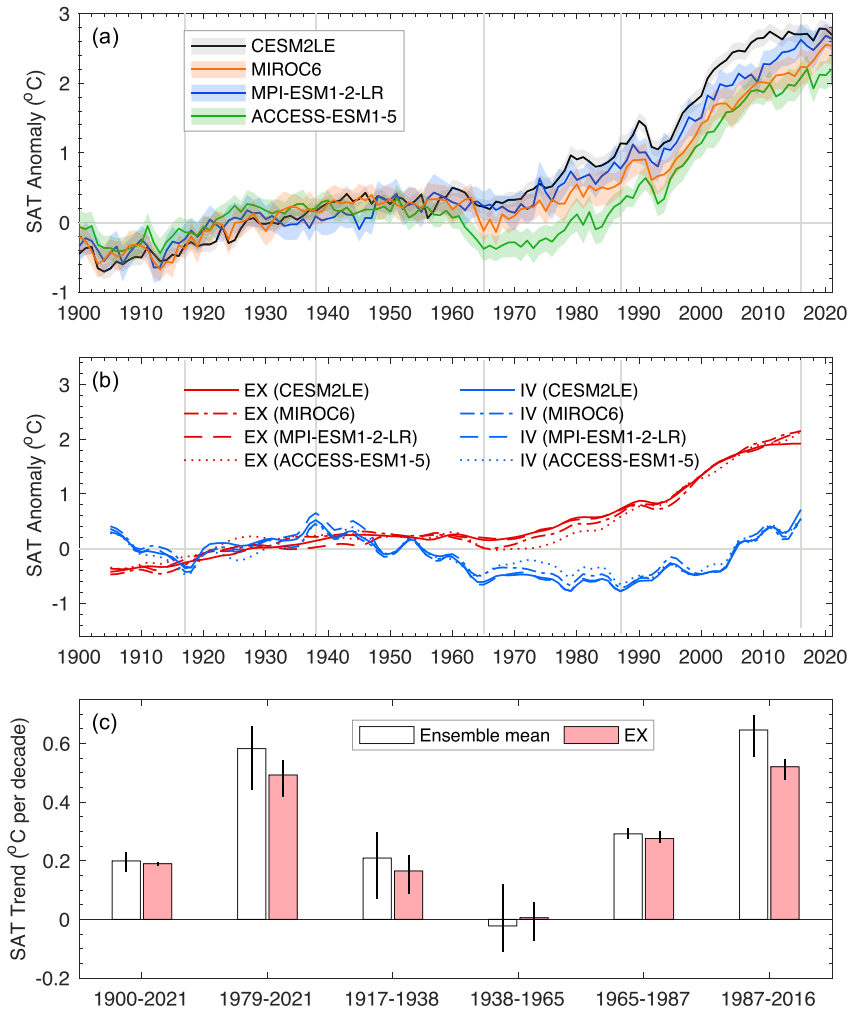

Figure 2. Inter-model differences in the forced signals and estimated forced components for CMIP6 ensembles. (a) Forced signals for Arctic-mean surface air temperature (SAT) anomalies (°C) from 1900 to 2021 obtained from ensemble means of CESM2LE (black line), MIROC6 (orange line), MPI-ESM1-2-LR (blue line), and ACCESS-ESM1-5 (green line) simulations, along with the respective inter-realization spreads (shadings). (b) Low-pass filtered time series of EX (red lines) and IV components (blue lines) in Arctic-mean BEST SAT anomalies estimated through linear regression using the forced signals in (a). The beginning and ending 5 years of low-pass filtered time series are not shown. (c) Linear trends (° C decade^{-1}) of low-pass filtered forced signals (white bars) and the EX components estimated using them (red bars) averaged over CESM2LE and three CMIP6 ensembles, with their spreads shown by vertical lines.

small ensemble sizes of single-forcing ensembles. This suggests that Arctic SAT responses to the historical external forcings are approximately linearly additive.

The EX component dominates the overall changes in observed Arctic SAT from 1900 to 2021 (Figures 1a and 1b), explaining ~80% of the total variance (which includes the long-term changes) and most of the long-term Arctic warming since 1900 (Figure 1c). The response to external forcing also accounts for much (~60%) of the rapid Arctic warming since 1979, consistent with Johannessen et al. (2004) and Nozawa et al. (2005) who examined only a few realizations and thus had difficulties in dealing with the large IV-induced spread. As shown in Figures 4c–4g, the forced trends over 1900–2021 are mainly caused by a combination of GHG-induced warming, AA-induced cooling, and warming induced by natural forcings, while the role of BBA is fairly minimal. The forcings in the EE runs mainly represents a long-term increase in solar radiation during the 20th century and a lull in volcanic activity from 1920 to 1960 and after the early 1990s (see the annual effective solar irradiance north of 30°N in Suo et al. (2013) and the annual stratospheric aerosol optical depth in Bokuchava & Semenov, 2021). The EE forcing contributes as much as the GHG forcing during 1979–2021 and even more than the GHG forcing during the rapid warming from 1987 to 2016, which mainly reflects the

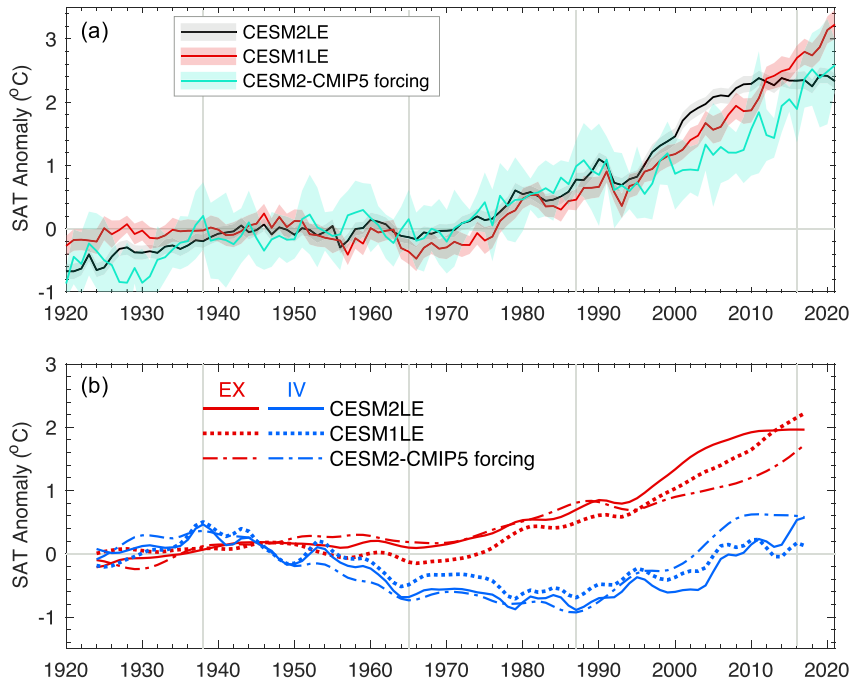

Figure 3. Forced signals and forced components estimated using CESM1LE, CESM2LE, and CESM2-CMIP5 ensembles. (a) Forced signals for Arctic-mean surface air temperature (SAT) anomalies (°C) from 1920 to 2021 obtained from ensemble means of CESM2LE (black line), CESM1LE (red line), and CESM2-CMIP5 forcing ensemble (cyan line), along with the respective inter-realization spreads (shadings). (b) Low-pass filtered time series of the EX (red lines) and IV components (blue lines) in Arctic-mean BEST SAT anomalies estimated through linear regression using the forced signals in (a). The beginning and ending 5 years of low-pass filtered time series are not shown. Because the CESM1LE simulations start from 1920, in this figure the reference state is defined as the 1921–1970 mean while it is defined as the 1901–1970 mean in the rest of the manuscript.

warming effect due to increased solar activity and the recovery from the cooling caused by the Pinatubo volcanic eruption in 1991.

Previous studies broadly agree that the early 20th century Arctic warming is caused by a combined effect of internal variability and anthropogenic and natural forcings, but it remains challenging to quantify their relative contributions (e.g., Bokuchava & Semenov, 2021; Fyfe et al., 2013; Johannessen et al., 2004; Suo et al., 2013; Svendsen et al., 2021). In our estimates, anthropogenic GHG and AA changes and natural forcing (mainly an increase in solar radiation and a lull of volcanic eruptions) during this period have similar contributions to the early 20th century warming from 1917 to 1938 (the red, blue and green bars in Figure 4c), but their combined effect only explains 33% of observed warming during 1917–1938, with the rest from internal variability (Figure 1c). Extending the period to 1910–1945 only leads to a small increase (to 41%) in the contribution by the forced component. Thus, our results align with the findings of Tokinaga et al. (2017) and Svendsen et al. (2018, 2021) and suggest that the early 20th century warming is driven mainly by internal variability. Some studies that compared the observed warming trend directly with specific forcing series (e.g., Bokuchava & Semenov, 2021) or single-forcing simulations of SAT without rescaling (e.g., Suo et al., 2013) may have overestimated the effect of external forcing in the early 20th century warming. If we skipped the rescaling, our estimated contribution by external forcing to Arctic warming during 1917–1938 would be 43% (instead of the current 33%). This illustrates the importance of the rescaling described in Section 2.3. Consistent with England et al. (2021), we also found that the mid-20th century Arctic cooling is dominated by internal variability (Figure 1c), as the AA-induced cooling is largely canceled by the GHG-induced warming (Figure 4c).

3.2. Sources of Internal Variability Responsible for the IV Component in Arctic SAT

The leading mode (EOF1) from an EOF analysis of the low-pass filtered local IV components in observed Arctic SAT during 1900–2021 indicates pan-Arctic warming that is stronger over the Eurasian Arctic extending from the

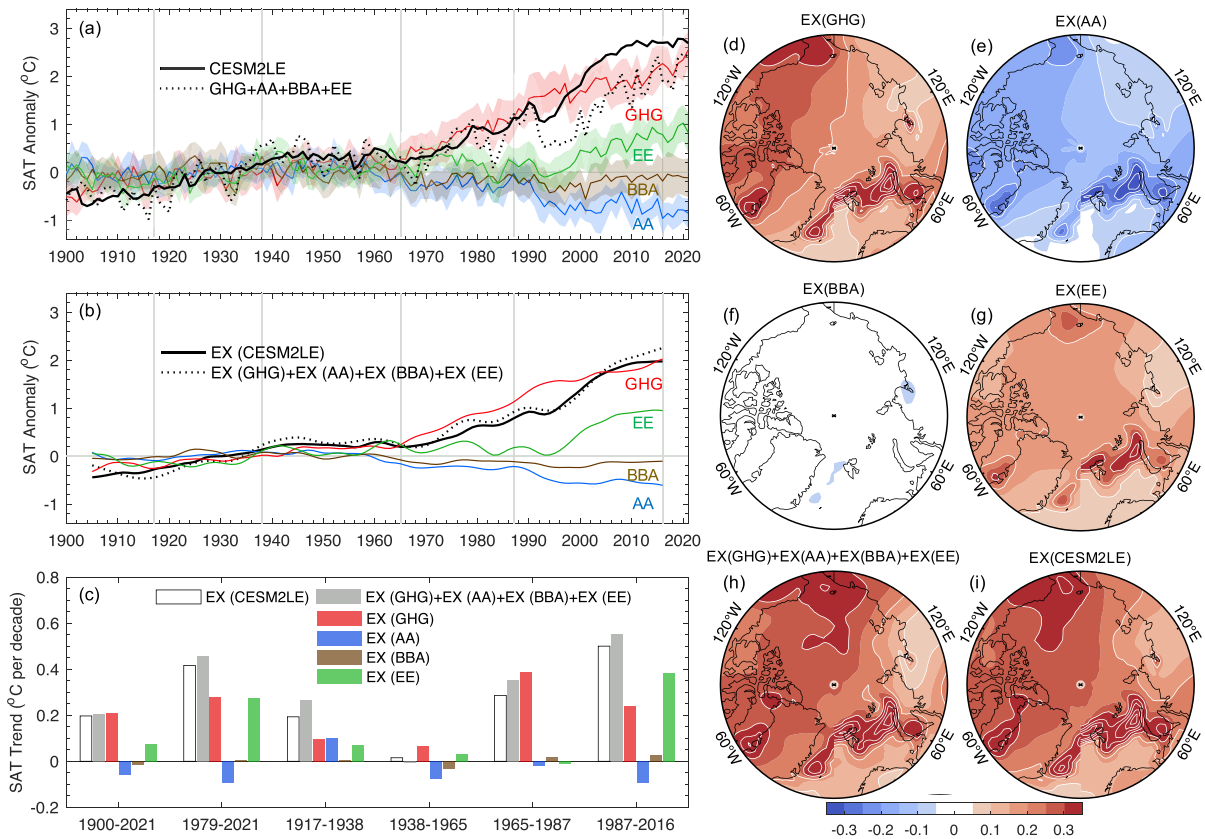

Figure 4. Forced Arctic surface air temperature (SAT) anomalies due to specific forcings. (a) Forced signals for Arctic SAT anomalies (°C) obtained from ensemble means of Community Earth System Model version 2 (CESM2) single-forcing runs (greenhouse gas (GHG), anthropogenic aerosols (AA), biomass burning aerosols (BBA), and EE are shown by red, blue, brown, and green lines, respectively, with inter-realization spreads shown by shadings), compared with their linear sum (black dotted line) and the forced signal obtained from the ensemble mean of CESM2LE (black solid line). (b) Low-pass filtered EX components in Arctic-mean Berkeley Earth Surface Temperature SAT anomalies (°C) estimated through linear regression using the forced signals in CESM2 single-forcing ensembles (GHG, AA, BBA, and EE are indicated by red, blue, brown, and green dashed lines, respectively), their linear sum (black dotted line), and the EX components estimated using the forced signal from CESM2LE (black solid line). The beginning and ending 5 years of the low-pass filtered time series are not shown. (c) Linear trends (°C decade^{-1}) of the low-pass filtered EX components estimated using the forced signals from CESM2 single-forcing ensembles (GHG, AA, BBA, and EE are indicated by red, blue, brown, and green bars, respectively), their linear sum (gray bars), and CESM2LE (white bars). (d–i) Trend patterns (°C decade^{-1}) of low-pass filtered EX components estimated using the forced signals in (d)–(g) CESM2 single-forcing ensembles, (h) their linear sum, and (i) CESM2LE over 1900–2021.

Siberian coast to the central Arctic (Figure 5c), which accounts for ~70% of the variance in the unforced Arctic SAT fields. The PC1 has a strong correlation with AMO ($r = 0.87$; Figure 5a). This correlation is primarily due to the IV component of AMO (dashed line in Figure 5a), which dominates the overall AMO changes during 1900–2021 and generally is in-phase with PC1 (purple line in Figure 5a). Nevertheless, the difference between the shading and the dashed line in Figure 5a indicates that the EX component contributes significantly to the total AMO since the mid-1940s with a cooling trend from 1940s to 1970s and a warming trend since the mid-1990s, consistent with previous analyses (e.g., Qin et al., 2020a). Thus, AMO's contribution to Arctic SAT changes might be overestimated if we used the total AMO instead of its unforced component. Regressing the unforced Arctic SAT against the unforced AMO reveals a pan-Arctic warming centered around the Kara Sea (Figure 5e), which is comparable to the EOF1 pattern (Figure 5c, $r = 0.81$, $p < 0.01$) with some regional differences (e.g., over Greenland). The SST pattern associated with the positive PC1 is characterized by basin-wide warming over the North Atlantic (Figure 6a), similar to the warm phase of unforced AMO (Figure 6b). Their pattern correlation coefficient is 0.53 over the entire globe ($p < 0.01$) and reaches 0.80 over the Atlantic domain (0–80°W, 55°S–60°N).

The second mode (EOF2), which explains ~10% of the variance in the unforced Arctic SAT fields, exhibits warming from northern Canada to Alaska and cooling from Svalbard to the Barents Sea (Figure 5d). As the warming is stronger and more extensive than the cooling, EOF2 represents weak warming averaged over the entire Arctic from 67° to 90°N. It is positively correlated with IPO ($r = 0.54$, $p < 0.01$), especially IPO's IV

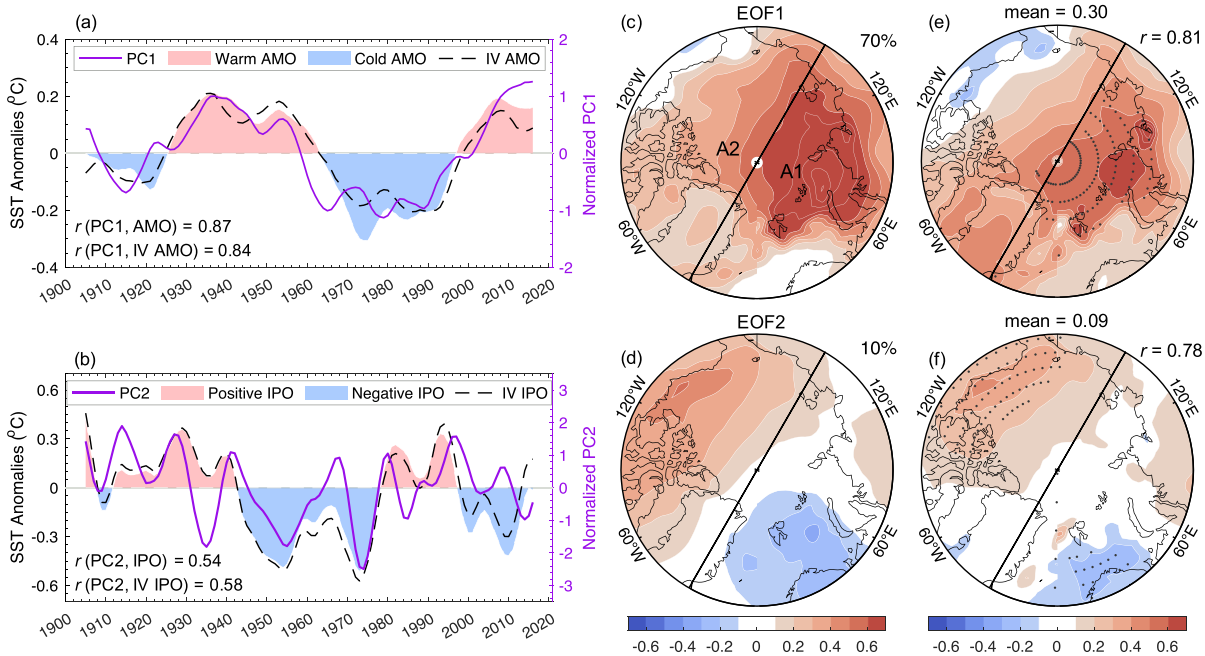

Figure 5. Leading modes of the unforced Arctic surface air temperature (SAT) anomalies. (a and b) Time series of first and second principal components (PC1 and PC2, purple lines) from the empirical orthogonal function analysis of low-pass filtered IV components of BEST SAT anomalies over the Arctic from 1900 to 2021 with the forced component being estimated using CESM2LE ensemble-mean Arctic-mean SAT through linear regression. Also shown in (a) are the Atlantic Multidecadal Oscillation (AMO) index (pink and blue shadings for warm and cold phases, respectively) and its IV component (dashed line), and in (b) the Interdecadal Pacific Oscillation (IPO) index (pink and blue shadings for positive and negative phases, respectively) and its IV component (dashed line). The beginning and ending 5 years are not shown. The correlation coefficient *r* is shown in the bottom left corner. (c and d) The corresponding spatial patterns (EOF1 and EOF2) with the explained variances (in %). (e and f) Regressed SAT (°C per standard deviation) onto normalized IV components of (e) AMO and (f) IPO shown by dashed lines in (a) and (b). The Arctic-mean SAT anomalies (°C) for one standard deviation of the index are shown above the panel. The stippling indicates statistical significance at the 5% level. The pattern correlation coefficient *r* between the patterns in (c) and (e), (d) and (f) is shown in the top right corner of (e), (f). All the correlations shown in this figure are statistically significant at the 5% level. The Arctic is divided into two areas by the straight black line: A1 (from 30°W to 150°E, mainly the Atlantic-Eurasian Arctic, on the lower-right side of the black line) and A2 (from 150°E to 30°W, mainly the North American-Pacific Arctic, on the upper-left side of the black line).

component ($r = 0.58$, $p < 0.01$), which accounts for most of the observed IPO during 1900–2021 (Figure 5b). The SST pattern associated with positive PC2 displays a warm anomaly in ECEP and cold anomalies in the extra-tropical Pacific (Figure 6d), resembling the positive phase of unforced IPO pattern (Figure 6e). Their pattern correlation coefficient is 0.91 ($p < 0.01$) over the Pacific domain (140°E–90°W, 55°S–60°N). The regressed pattern of Arctic SAT against the unforced IPO (Figure 5f) are highly correlated ($r = 0.78$, $p < 0.01$) with EOF2 pattern (Figure 5d), although regional differences exist.

These results strongly indicate that there are close associations between EOF1 and unforced AMO and between EOF2 and unforced IPO. To understand how they are interconnected, we examine the associated changes in precipitation (Figure 6), horizontal (Figure 7) and meridional atmospheric circulations (Figure 8). Figures 6–8 also show the differences between the idealized AMO^+ and AMO^- pacemaker simulations (idealized IPO^+ and IPO^- pacemaker simulations) that represent the impact of unforced AMO^+ (IPO^+) relative to the impact of unforced AMO^- (IPO^-). The simulated Arctic SAT differences are shown in Figure 9. The SST differences between the idealized AMO^+ and AMO^- (IPO^+ and IPO^-) pacemaker simulations are very similar to the SST anomalies associated with positive PC1 (PC2) over the North Atlantic (Pacific), with a significant pattern correlation reaching 0.74 (0.77).

Associated with positive PC1 or warm AMO, the reanalysis data shows a high-pressure anomaly in the upper troposphere at high latitudes in the North Hemisphere (contours in Figures 7a and 7b) but a low-pressure anomaly near the surface stretching from the northern North Atlantic to the Barents and Kara Seas (shadings in Figures 7a and 7b) above anomalous warm SSTs (shadings in Figures 6a and 6b), which suggests ascending anomalies in the Atlantic-Eurasian Arctic. Accordingly, we find a weakening in the Polar cell between 50° and 80°N in reanalysis data sets during positive PC1 and AMO (Figures 8a and 8b), which can lead to anomalous low-level southerlies

10.1029/2023EF003734

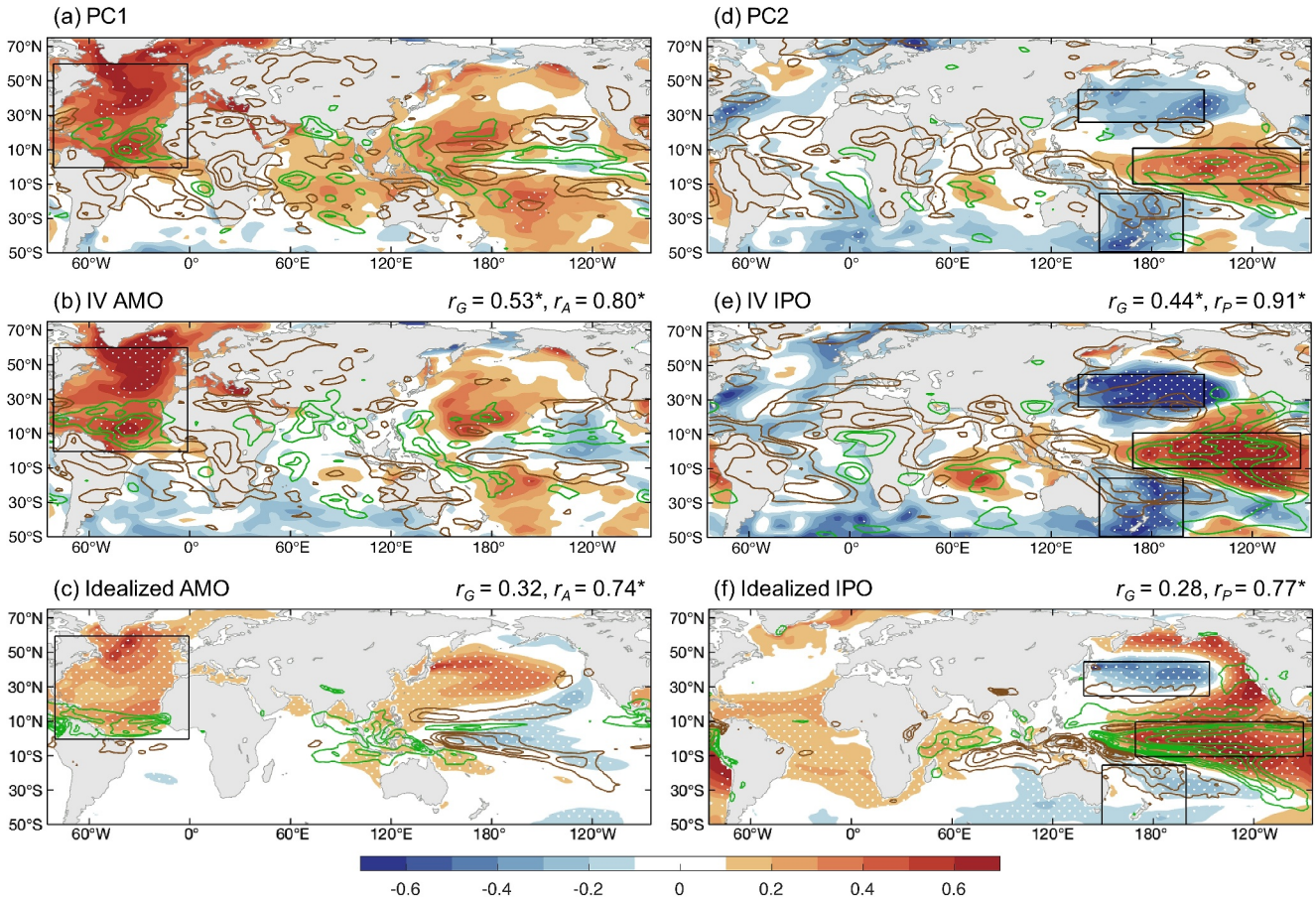

Figure 6. Sea surface temperature (SST) and precipitation associated with the unforced Arctic warming. (a, b, d, e) Correlation coefficients between low-pass filtered anomalies of observed SST (shading) and precipitation (contours; positive green and negative brown with an interval of 0.2) at each grid point with (a) PC1 and (d) PC2 (purple lines in Figures 5a and 5b), and with the IV components of (b) Atlantic Multidecadal Oscillation and (e) Interdecadal Pacific Oscillation (dashed lines in Figures 5a and 5b). (c, f) Ensemble-mean differences in SST (shading; °C) and precipitation (contours; positive green and negative brown with an interval of 0.2 mm/day) between (c) the idealized AMO^+ and AMO^- pacemaker simulations and (f) the idealized IPO^+ and IPO^- pacemaker simulations. The stippling indicates that the correlation or difference shown by shading is statistically significant at the 5% level. In (b), (c), (e), (f), pattern correlation coefficients with the SST pattern in a (d) over the globe (r_G), Atlantic domain (80°W–0°, 50°S–60N°, r_A), and Pacific domain (140°E–90W°, 50°S–60N°, r_P) are shown, with the superscript star indicating statistical significance at the 5% level. The North Atlantic (80°W–0°, 0°–60N°) are outlined in the left column. The equatorial central-eastern Pacific (170°E–90W°, 10°S–10°N), NWP (140°E–145W°, 25°N–45°N), and SWP (150°E–160W°, 50°S–15°S) are outlined the in right column.

and thus warm advection into the marginal Arctic (Figures 7a and 7b). Meanwhile, related to precipitation increases in the tropical North Atlantic (contours in Figures 6a and 6b) caused by the interhemispheric SST gradient (shadings in Figures 6a and 6b), the ascending branch of the Hadley cell strengthens around 10°N during positive PC1 and AMO (Figures 8a and 8b), consistent with a northward displacement of the Atlantic Intertropical Convergence Zone (ITCZ) in response to a warm AMO as previously proposed (e.g., Peings & Magnusdottir, 2016). Such enhanced precipitation and displaced ITCZ can generate upper-level divergence and a Rossby wave train into mid-high latitudes, resulting in high pressure anomalies over northern Eurasia from the surface to upper troposphere (e.g., Okumura et al., 2001). Thus, associated with positive PC1 and AMO, we find high pressure anomalies around northern Eurasia both at the surface and in the upper troposphere in reanalysis data (shadings and contours in Figures 7a and 7b), which causes southwesterly anomalies from the North Atlantic toward the Barents-Kara Sea along the coast of Northern Europe (vectors in Figures 7a and 7b), bringing anomalous heat and moisture advection into the Arctic. Furthermore, the subpolar warming in the North Atlantic associated with positive PC1 and AMO (shadings in Figures 6a and 6b) can result in anomalous oceanic heat transport by ocean currents from the North Atlantic into the Arctic such as the Barents-Kara Sea (Beitsch et al., 2014; Bengtsson et al., 2004; Goosse & Holland, 2005), which also favors Arctic warming especially in the Atlantic-Eurasian sector.

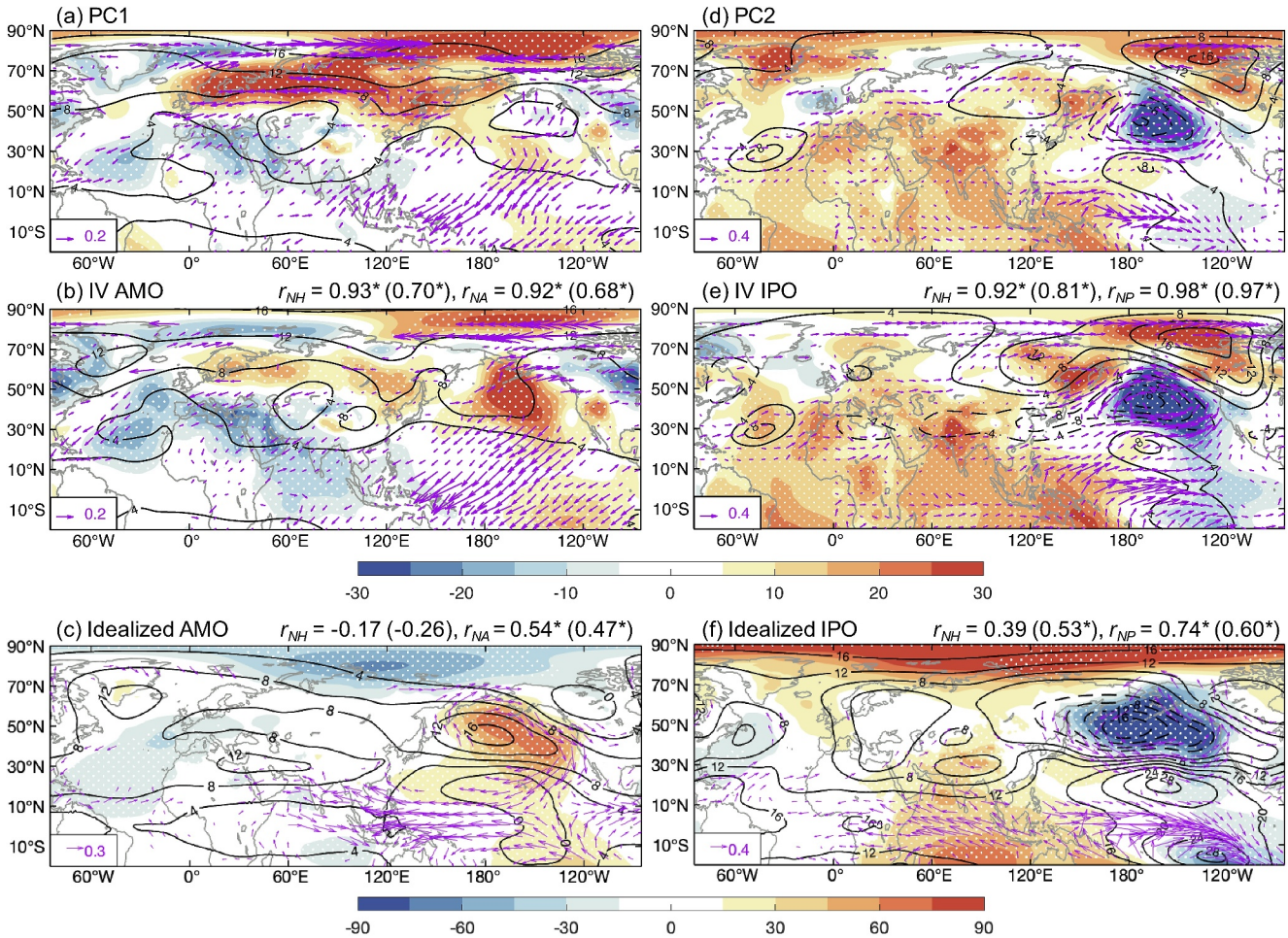

Figure 7. Horizonal atmospheric circulation anomalies associated with the unforced Arctic warming. (a, b, d, e) Regressed maps of sea surface pressure (SLP; shadings; Pa per standard deviation), 200-hPa geopotential height (Z200; contour interval = 4 gpm per standard deviation; positive solid and negative dashed), and 850-hPa horizonal wind anomalies in ERA-20C and ERA5 reanalysis (UV850; vectors; m/s per standard deviation) at each grid point onto (a) PC1 and (d) PC2, and the IV components of (b) Atlantic Multidecadal Oscillation and (e) Interdecadal Pacific Oscillation. (c), (f) Ensemble-mean differences in sea level pressure (SLP) (shadings; Pa), Z200 (contour interval = 4 m; positive solid and negative dashed) and UV850 (vectors; m/s) between (c) the idealized AMO^+ and AMO^- pacemaker simulations and (f) the idealized IPO^+ and IPO^- pacemaker simulations. The stippling indicates that the SLP anomaly or difference is statistically significant at the 5% level. In (b), (c), (d)–(f), the Z200 pattern correlation coefficients with a (d) over the northern hemisphere (r_{NH}), North Atlantic (r_{NA}), and North Pacific (140°E–90W°, 0°–60N°, r_{NP}) are shown, with the superscript star indicating the statistical significance at the 5% level; likewise, the SLP pattern correlation coefficients are shown in the parentheses.

Similar to the observational and reanalysis regression results, the difference between the idealized AMO^+ and AMO^- pacemaker simulations indicates anomalous warm SSTs extending from the North Atlantic to the Barents Sea (Figure 6c), decreased surface pressure and increased upper-level pressure over the North Atlantic and Eurasian Arctic (Figure 7c), weakening of the Polar cell (Figure 8c), and pan-Arctic warming (Figures 9a and 9c). This suggests that the unforced AMO is capable of causing the relationship with EOF1, and EOF1 largely represents the influence of the unforced AMO on the Arctic SAT. However, in the difference between the idealized AMO^+ and AMO^- simulations, Arctic warming spreads across the entire Arctic except the Greenland Sea (Figure 9c), unlike the warming centered around the Kara Sea in EOF1 (Figure 5c) and the observational regression (Figure 5e). Moreover, as the difference between the idealized AMO^+ and AMO^- experiments shows a ~0.25°C increase in the SST averaged over the North Atlantic (Figure 6c) and a ~0.25°C increase in the Arctic-mean SAT (Figure 9a), the simulated Arctic warming response to 1°C SST increase averaged over the North Atlantic is approximately 1°C. This magnitude is much smaller than the corresponding regression in the observation: a 1°C increase in the North Atlantic-mean SST is associated with a 2.5°C Arctic warming. This lower response may be partly caused by the extensive sea-ice cover in the simulations due to the use of PI radiative forcing. Excessive sea

10.1029/2023EF003734

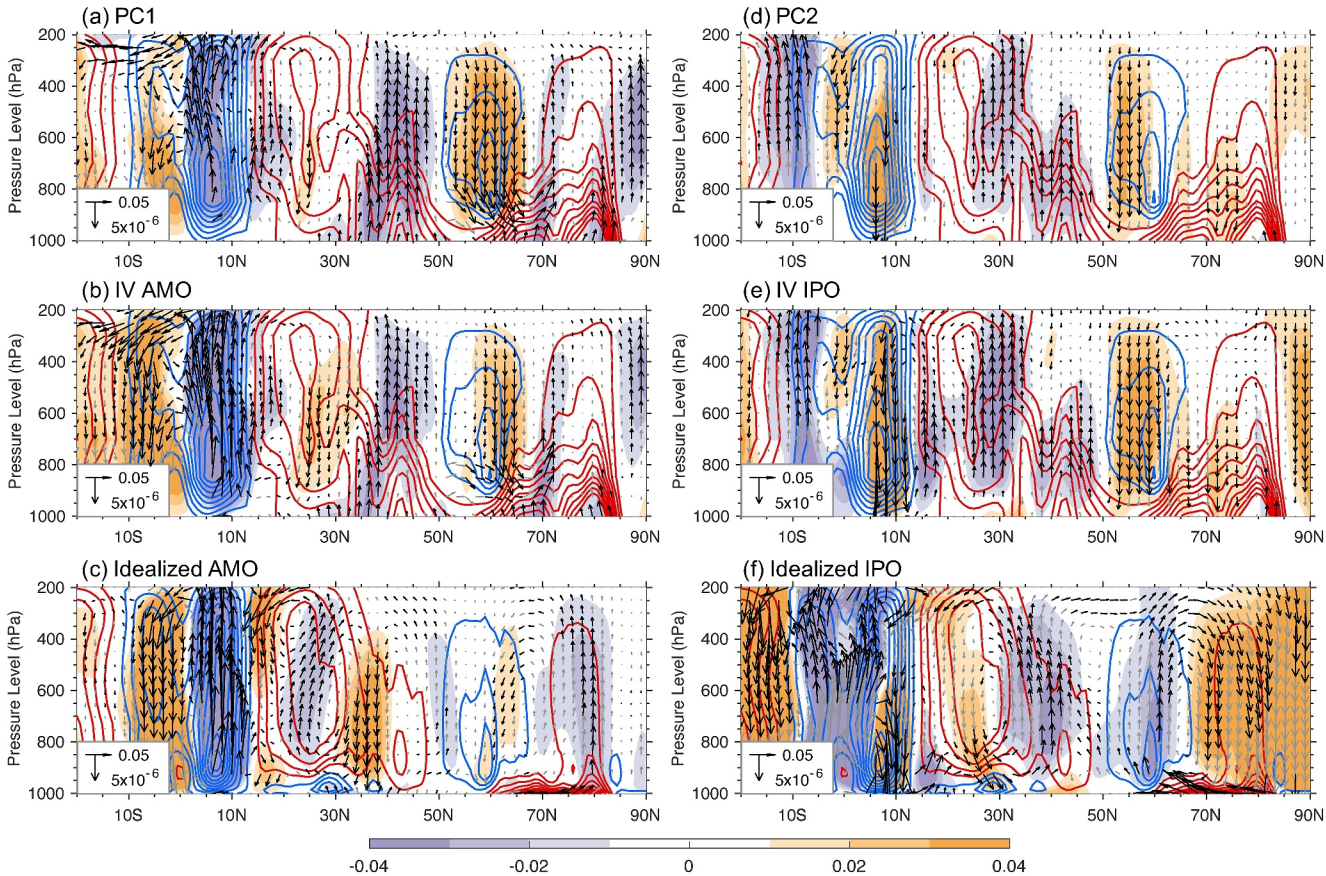

Figure 8. Meridional circulation anomalies associated with the unforced Arctic warming. (a, b, d, e) Zonal-mean profiles of regressed vertical pressure velocity and meridional velocity anomalies from ERA-20C and ERA5 reanalysis (vectors; hPa/s and m/s per standard deviation, respectively) onto (a) PC1 and (d) PC2, and the IV components of (b) Atlantic Multidecadal Oscillation and (e) Interdecadal Pacific Oscillation. (c), (f) Zonal-mean profiles of ensemble-mean differences in vertical pressure velocity and meridional velocity (vectors; hPa/s and m/s, respectively) between (c) the idealized AMO^+ and AMO^- pacemaker simulations and (f) the idealized IPO^+ and IPO^- pacemaker simulations. The black vector highlights the regressed anomaly or difference statistically significant at the 5% level in vertical pressure velocity or meridional velocity. Shadings denote vertical pressure velocity anomalies (10^{-4} hPa/s per standard deviation) in (a), (b), (d), (e) and differences (10^{-4} hPa/s) in (c), (f), with upward (downward) motions shown in purple (orange). Contours denote the climatology of vertical pressure velocity (blue for ascending and red for descending with an interval of 0.4×10^{-4} hPa/s).

ice can dampen Arctic warming especially over the Eurasian sector by cutting off the amplifying feedbacks associated with sea-ice variations (Deng & Dai, 2022). In addition, although the simulated difference shows increased precipitation in the tropical North Atlantic (Figure 6c) similar to the reanalysis data regressions, the surface high pressure response is weak over Eurasia compared with the reanalysis (Figures 7b and 7c). The simulated difference therefore cannot capture the anomalous warm advection from the North Atlantic into the Arctic, which may also contribute to the underestimation of the warming response in simulations.

With positive PC2 and IPO, tropical precipitation is enhanced in the central Pacific (contours in Figures 6d and 6e) in response to the warm SSTs over ECEP (shadings in Figures 6d and 6e), which triggers upper-level divergence anomalies in the subtropical Pacific and thus generates an atmospheric teleconnection from the tropical Pacific across the North Pacific to northern Canada with a quasi-barotropic structure at mid-high latitudes (Figures 7d and 7e). A similar wave-train structure originating from excessive tropical convection is captured by the differences between the idealized IPO^+ and IPO^- pacemaker experiments (Figures 6f and 7f). The 200-hPa geopotential height and SLP difference patterns between the idealized IPO^+ and IPO^- simulations over the North Pacific roughly resemble the regressed patterns in the reanalysis ($r = 0.74$ and 0.60, $p < 0.01$). Similar wave-train like pattern has also been observed in atmospheric model simulations forced by tropical SST anomalies characterized by ECEP warming (Deser & Phillips, 2009; Tokinaga et al., 2017). Their paralleled experiments forced by the positive IPO-like SST trend and its tropical component suggested that the tropical forcing of IPO explains the majority of the wave-train like pattern across the North Pacific, as well as the Pacific-North American Arctic warming related to

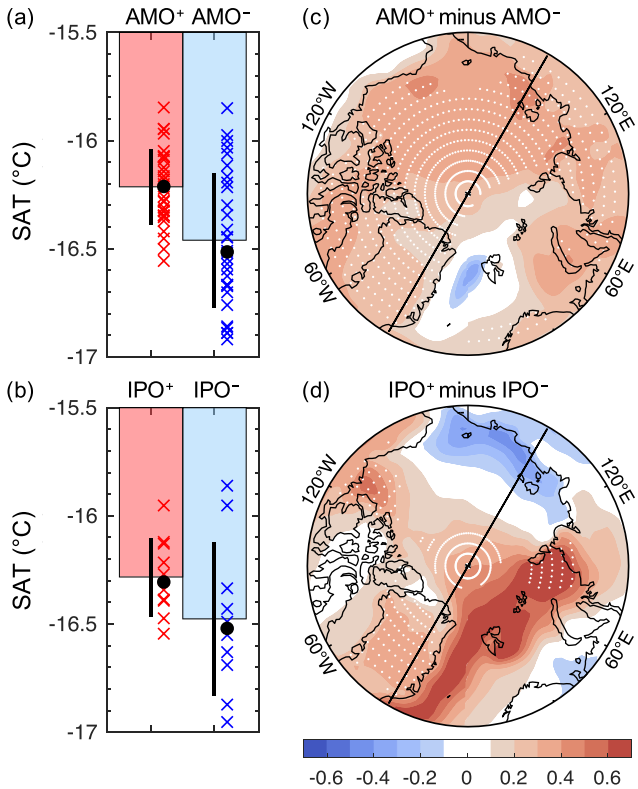

Figure 9. CESM1-simulated Arctic surface air temperature (SAT) responses in idealized pacemaker experiments. Arctic-mean SAT (°C) in (a) idealized AMO^+ and AMO^- pacemaker simulations and (b) idealized IPO^+ and IPO^- pacemaker simulations by CESM1, with bars showing the ensemble means, vertical black lines showing the ±1 standard deviation ranges, crosses showing the individual runs, and dots showing the medians. SAT differences (°C) between (c) the idealized AMO^+ and AMO^- pacemaker simulations and (d) the idealized IPO^+ and IPO^- pacemaker simulations over the Arctic. The stippling indicates that the difference is statistically significant at the 5% level.

IPO. The deepened Aleutian Low (shadings in Figures 7d–7f), enhances southeasterly winds along the west coast of North America (vectors in Figures 7d–7f) and advects anomalous warm and moist air to the Arctic, promoting Arctic warming in the North American-Pacific sector. In the reanalysis and simulations, in accordance with positive surface pressure anomalies occurred over the majority of Arctic regions during positive PC2 and IPO (shadings in Figures 7d–7f), the descending branch of the Polar cell within the Arctic strengthens (Figures 8d–8f), which may also contribute to Arctic warming by adiabatic heating. The Arctic is ∼0.2°C warmer in the idealized IPO^+ experiment than in the idealized IPO^- experiment (Figure 9b), in response to a ∼1°C increase in the SST difference of ECEP minus the sum of NWP and SWP (Figure 6f). This warming magnitude is comparable to that in observational regressions: a ∼0.3°C Arctic warming corresponds to a 1°C increase in the SST difference of ECEP minus the sum of NWP and SWP. The above results suggest that the poleward-propagating wave train originating from excessive tropical convections and the resultant Arctic warming are robust responses to the positive phase of unforced IPO, and PC2 represents the influence of unforced IPO on Arctic SAT. However, the simulated SAT difference indicates stronger warming in the Atlantic sector (Figure 9d) rather than in the North American-Pacific sector as in EOF2 (Figure 5d) or in the observational regressions (Figure 5f). This is probably due to the differences in the IPO-related SST changes in simulations and observations over the North Atlantic (Figures 6d–6f), which further results in different atmospheric circulation responses from the North Atlantic to Eurasia (Figures 7d–7f). The small ensemble size of the idealized IPO pacemaker experiments may also introduce uncertainty regarding the spatial pattern of Arctic warming response.

To quantify the AMO- and IPO-related Arctic SAT changes, their associated Arctic-mean SAT time series are reconstructed by multiplying the normalized IV component of the AMO or IPO index by the corresponding Arctic-mean SAT anomalies per standard deviation of the index (shown above Figures 5e and 5f). We find that the Arctic-mean SAT changes associated with unforced AMO (orange line in Figure 10a) largely explains the multidecadal swings in the unforced component of the observation, including cooling periods before 1917 and from 1938 to 1965 and warming periods from 1917 to 1938 and after 1987, with a maximum of ∼0.4°C around 1940 and a minimum of ∼−0.4°C around 1975. In contrast, the IPO only induces small fluctuations in Arctic-mean SAT on decadal time scales (blue line in Figure 10a), mainly due to the cancellation of the dipole structure of EOF2 (Figure 5f). As expected, the reconstructed time series (orange and blue lines in Figure 10a) are unrelated to the EX component of the observed Arctic SAT ($r = 0.09$ and -0.07, respectively), suggesting that the influences of the unforced AMO and IPO are largely independent from the forced response.

The combined effect of AMO and IPO explains approximately half of the early 20th century warming and mid-20th century cooling in observations (Figures 1c and 10b). It is primarily due to a warm AMO peak in the 1930s and its switch to a cold phase until the 1970s (Figure 5a). Moreover, the unforced warming in the North Atlantic since the 1970s accounts for ∼32% of the observed Arctic warming trend from 1979 to 2021 and ∼80% of its unforced component (Figures 1c and 10b). The positive-to-negative IPO transition around 2000 (Figure 5b) partially offsets the AMO-induced Arctic warming during 1987–2016 (Figure 10b).

We emphasize that while IPO's impact on Arctic-mean SAT may be small due to the opposite dipole structure in Arctic SAT (Figure 5d), its impact on regional SAT over the North American-Pacific sector could be large. Figure 11 shows that IPO's influence (blue lines) is larger in the North American-Pacific Arctic (A2) than in the Atlantic-Eurasian Arctic (A1) sector, whereas AMO's influence (orange lines) is relatively small in the North American-Pacific Arctic. The IV component of SAT in the Atlantic-Eurasian Arctic comes mainly from AMO's IV component (Figure 11a), whereas for the North American-Pacific Arctic and Arctic-mean it results from both IPO and AMO and other variability (Figure 11b). This results in stronger multidecadal variations in the observed SAT

10.1029/2023EF003734

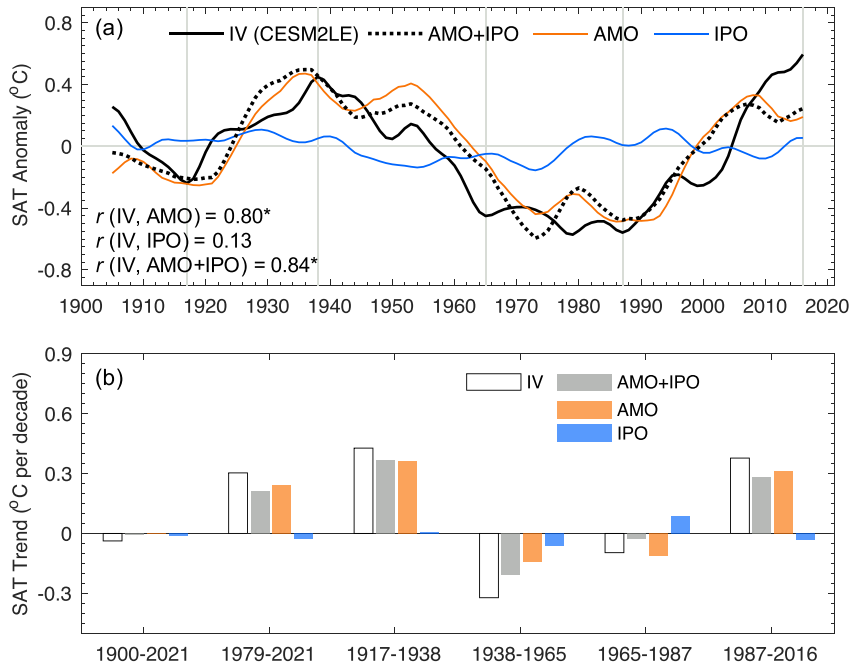

Figure 10. Unforced Arctic surface air temperature (SAT) changes due to Atlantic Multidecadal Oscillation (AMO) and Interdecadal Pacific Oscillation (IPO). (a) Reconstructed Arctic-mean SAT anomalies (°C) from 1900 to 2021 calculated using normalized IV components of AMO (orange line) and IPO (blue line) multiplied by the associated Arctic-mean SAT anomalies (°C per standard deviation), with the black dotted line showing their sum. The black solid line shows the low-pass filtered IV components in Arctic-mean SAT anomalies using Berkeley Earth Surface Temperature data set and CESM2LE for estimating the forced component (see black solid line in Figure 1b). The beginning and ending 5 years of the low-pass filtered time series are not shown. The correlation coefficients between the time series are given in the bottom left corner, with the superscript star indicating statistical significance at the 5% level. (b) Linear trends (°C per decade) of the black solid line (white bars), black dotted line (gray bars), orange line (orange bars), and blue line (blue bars) in (a) for different periods.

over the Atlantic-Eurasian Arctic and more decadal fluctuations in the observed SAT over the North American-Pacific Arctic (black solid lines in Figures 11a and 11b). Due to EOF1's stronger loading over the Eurasian Arctic (Figure 5c), unforced components of the early 20th-century warming from 1917 to 1938 and recent rapid warming since 1987 are relatively pronounced in the Atlantic Eurasian Arctic (Figures 11c and 11d). On the other hand, as externally forced warming is faster in the North American-Pacific Arctic than in the Atlantic-Eurasian Arctic in recent decades (black dashed lines in Figures 11a and 11b), the forced response contributes more to the rapid warming since 1979 or from 1987 to 2016 in the North American-Pacific Arctic (Figures 11c and 11d).

The forced and unforced Arctic SAT changes are generally greater during winter than during summer (white bars in Figure 12), which is consistent with the stronger warming effect by sea-ice loss and other Arctic positive feedbacks in the cold season (Dai et al., 2019; Jenkins & Dai, 2022). The GHG-induced Arctic warming and other forced components (except the cooling by AA in the mid-20th century) are also substantially stronger in winter than in summer (Figures 12a and 12c), which is not surprising given the stronger Arctic feedbacks in winter. Similarly, AMO and IPO's influences on Arctic SAT are much weaker in summer than in winter (Figures 12b and 12d), also likely due to stronger winter positive feedbacks associated with sea-ice variations and changes. In particular, the mid-20th century cooling dominated by internal variability is absent in summer (white bars in Figure 12d). Presumably, this is also due to weak Arctic feedbacks in the warm season (Jenkins & Dai, 2022). Thus, both the externally forced and internally generated SAT changes over the Arctic are much stronger in winter than in summer, likely due to the stronger effects from sea-ice loss and other Arctic feedbacks in winter and the stabilizing effect of the Arctic Ocean open water surfaces in summer.

4. Summary and Discussion

To improve quantitative understanding of the contributions from external forcing and internal variability to observed Arctic (67°–90°N) warming, we used a 100-member CESM2LE and a rescaling method to estimate the

10.1029/2023EF003734

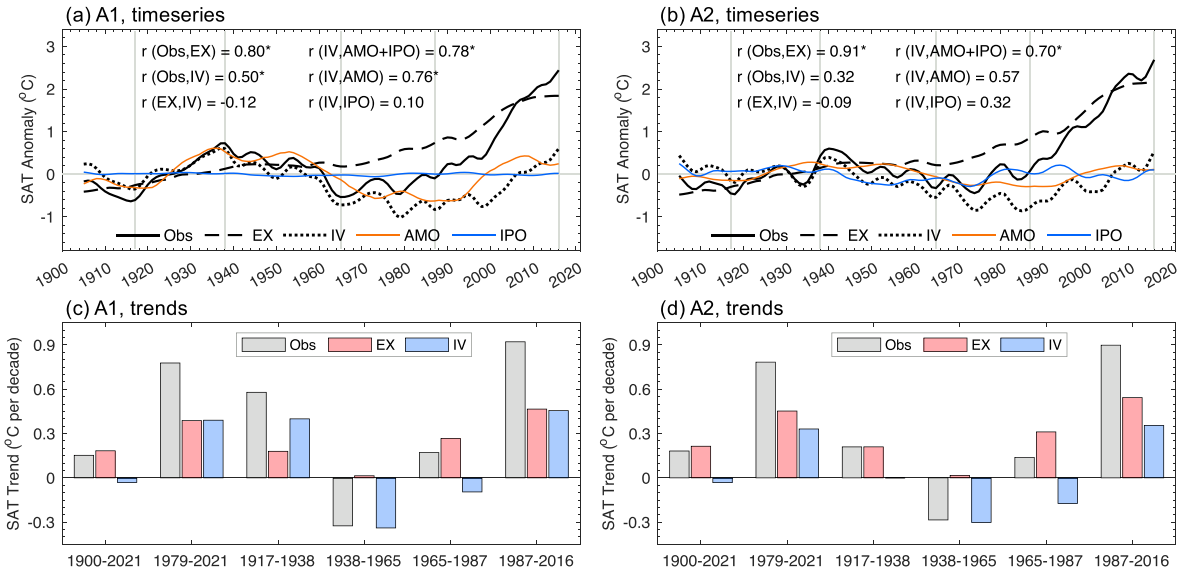

Figure 11. Differences between the Atlantic-Eurasian Arctic and North American-Pacific Arctic. (a and b) Low-pass filtered time series of regional Berkeley Earth Surface Temperature (BEST) surface air temperature (SAT) anomalies (°C; black solid lines) averaged over (a) A1 and (b) A2 (A1 denotes the Atlantic-Eurasian Arctic sector and A2 denotes the North American-Pacific Arctic sector as shown in Figure 5c) and the EX (black dashed lines) and IV components (black dotted lines) estimated through linear regression using CESM2LE ensemble-mean SAT time series averaged over A1 and A2 as the forced signal, respectively, and regional SAT anomalies reconstructed by normalized IV components of Atlantic Multidecadal Oscillation (orange lines) and Interdecadal Pacific Oscillation (blue lines) multiplied by the associated SAT anomalies (°C per standard deviation) averaged over (a) A1 and (b) A2, respectively. The beginning and ending 5 years of the low-pass filtered time series are not shown. The correlation coefficients between the time series within each panel are given, with the superscript star indicating statistical significance at the 5% level. (c and d) Linear trends (°C per decade) of regional BEST SAT timeseries averaged over (c) A1 and (d) A2 (gray bars) and the EX (red bars) and IV (blue bars) components.

EX and IV components in Arctic SAT changes from 1900 to 2021, and examined their temporal and spatial patterns, seasonal differences, and contributions to observed warming trends over different sub-periods. Our estimated EX component is not strongly affected by the choice of the observational SAT data set and the model ensemble, and it exhibits a long-term warming trend as a result of the GHG forcing and natural forcing and cooling due to AA forcing, with some slowdown from the 1940s–1960s and a pause in the early 1900s. We find that the forced response dominates the overall changes in Arctic SAT from 1900 to 2021. In contrast, the IV component shows no significant trend from 1900 to 2021, but it significantly influences the decadal-to-multidecadal trends in Arctic SAT. Our estimate further shows that the forced component accounts for almost all of the Arctic long-term warming from 1900 to 2021 and much (~60%) of the rapid warming since 1979, explaining 80% of the total variance during 1900–2021. However, the early 20th century Arctic warming from 1917 to 1938 resulted primarily from internal variability (67%) and second from external forcing (33%), and the mid-20th century Arctic cooling from 1938 to 1965 resulted mainly from internal variability (104%) as the GHG and other forcing-induced warming is canceled out by the AA-induced cooling. The rapid Arctic warming since 1987 is a combined effect of internal variability (mainly a negative-to-positive phase transition of the unforced AMO) and external forcing (mainly increases in GHG and solar activity, and the recovery from Pinatubo-induced cooling at the beginning of the 1990s). The small ensemble size (15) of single-forcing experiments might not fully eliminate the impact of internal variability in the ensemble mean, thus the attributions to individual forcings may require additional verification. Both forced and unforced changes are stronger in winter than in summer likely due to the larger effects from sea-ice loss on the atmosphere and stronger Arctic positive feedbacks in the cold season, as well as the stabilizing effect of Arctic Ocean open water surfaces in summer; however, the percentage contributions by external forcing to Arctic warming is greater in summer than in winter due to the greatly weakened impact on summer Arctic SAT by internal variability.

The unforced changes in Arctic SAT can largely be attributed to two leading modes. The first mode, which accounts for 70% of the unforced variance, is pan-Arctic warming characterized by stronger warming over the Eurasian Arctic, possibly caused by a warm phase of unforced AMO. A warm-phase AMO can warm the Arctic by weakening the Polar cell in the Atlantic-Eurasian sector and anomalous oceanic heat transport from the North

10.1029/2023EF003734

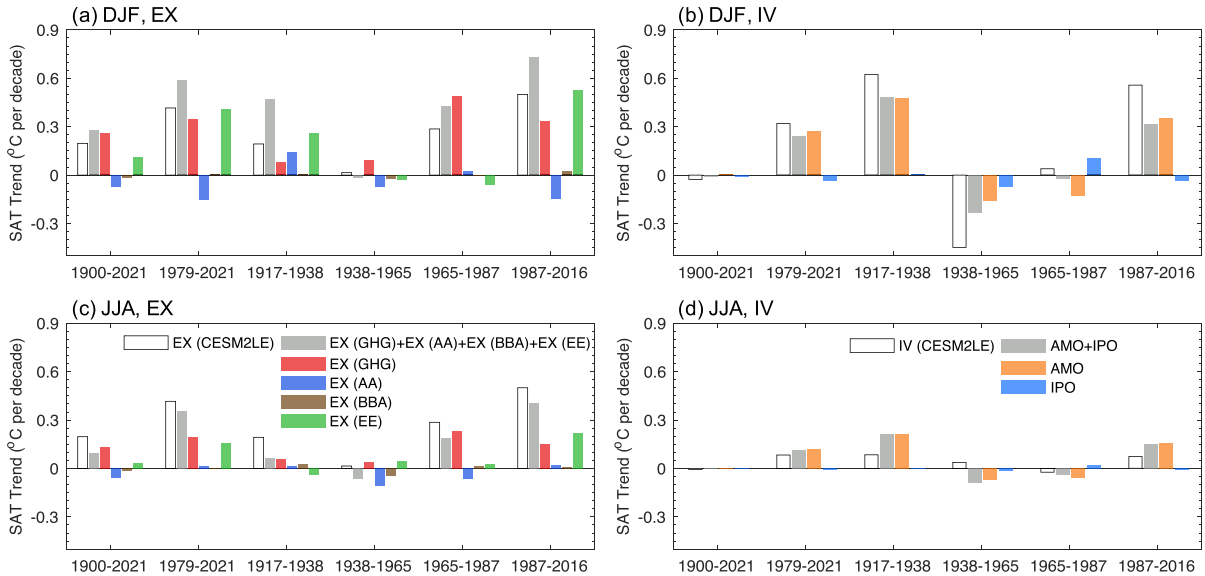

Figure 12. Differences Arctic-mean surface air temperature (SAT) trends between winter and summer. Similar to Figures 4c and 10b, but for the SAT during (a, b) winter (December to February, DJF) and (c, d) summer (June to August, JJA), instead of the annual-mean SAT. The forced signal used in regressions are (a, b) DJF-mean and (c, d) JJA-mean Arctic-mean SAT time series from CESM2LE ensemble mean and Community Earth System Model version 2 single-forcing ensemble mean. The left panels show the forced SAT trends due to different external forcings, while the right panels show the unforced SAT trends due to unforced Atlantic Multidecadal Oscillation and Interdecadal Pacific Oscillation over different periods.

Atlantic to the Arctic. The second mode exhibits relatively weak warming averaged over the entire Arctic with warming over the North American-Pacific sector and cooling over the Atlantic sector; it explains 10% of the unforced variance and is significantly correlated with the unforced IPO. A positive-phase IPO is characterized by excessive ECEP precipitation, whose latent heating triggers a poleward-propagating atmospheric wave train across the North Pacific, deepening the Aleutian Low, bringing more warm and moist air into the Pacific-North American Arctic, and resulting in adiabatic heating over the Arctic. Coupled pacemaker simulations by CESM1 with idealized AMO- or IPO-relatied SST anomalies specified only in their respective domain largely confirm the results based on observations and ERA5 data that the positive-phase AMO and IPO are more favorable for Arctic warming than the negative AMO and IPO. However, the warming pattern over the Arctic is not entirely consistent between observations and simulations, and the AMO-related warming is much weaker in simulations than in observations. This may be related to the excessive sea-ice cover in the pacemaker simulations with preindustrical radiative forcing which could dampen Arctic response to SST forcing, and the unrealistic SST response in the other ocean basin, which can affect the overall impacts on the Arctic. Further research is needed on the muted response. We estimated that the AMO dominates the unforced components of Arctic warming during 1979–2021, 1917–1938, and 1987–2016, especially over the Eurasian Arctic and in winter. This finding corroborates previous studies suggesting that the AMO dominates the unforced Arctic variations (e.g., Beitsch et al., 2014; Cai et al., 2021; Chylek et al., 2009, 2014; Goosse & Holland, 2005; Zhang, 2015), although the exact explained variance is divergent in these studies. This may partly because that they did not separate the observed AMO into the forced and unforced components and thus cannot precisely estimate the contributions from internal variability inherent in the North Atlantic. Using different methods to derive the IV components of AMO and IPO may also result in variations in the quantified numbers.

Our result differs from some earlier studies indicating that a positive-phase IPO was the major cause of the early 20th century warming in the Arctic (Svendsen et al., 2018). The experiment by Svendsen et al. (2018) is driven by wind observations over the Indo-Pacific, which may include not only the atmospheric response to IPO but also the influences from external forcing and AMO (Qin et al., 2020b); their estimates therefore cannot clearly separate the roles of IPO, AMO, and external forcing. On the other hand, our finding seems to contradict previous studies suggesting that the ECEP cooling trend (corresponding to a positive-to-negative phase transition of the IPO) drives the observed Arctic warming and sea-ice loss since 1979 (e.g., Ding et al., 2014, 2019). Ding et al. (2014) detected a coupling mode between cold ECEP and high pressure around Greenland using maximum covariance

analysis of observational and reanalysis data that intensified from 1979 to 2012 with the fastest rates occurring in the 1990s. Atmospheric model simulations forced by the observed SST in the tropics from 1979 to 2012 (including a cooling trend in ECEP) can produce a trend pattern with a wave-train structure similar to the observations, originating in the tropical Pacific and resulting in high pressures over northern Canada and Greenland (Ding et al., 2014). However, their simulated Arctic warming is much weaker than that in observations and is mainly over the Pacific Arctic whereas the observed warming trend is maximum over the Eurasian Arctic (Ding et al., 2014). In fact, the ECEP cooling trend from 1979 to 2012 emphasized by Ding et al. (2014) concurs with a negative-to-positive phase transition of AMO. A negative IPO-like pattern in the Pacific is a robust response to a warm AMO (Figure 6c), and many studies showed that the North Atlantic warming in recent decades can lead to an unprecedented increase in Pacific trade winds, which accounts for ~60% of the tropical Pacific cooling since 1979 (e.g., Cai et al., 2019; Li et al., 2016; McGregor et al., 2014; Meehl et al., 2021). Thus, perhaps Ding et al.'s statistical estimates of the IPO's influence include some contributions from the concurring AMO changes. It is also possible that our EOF1 includes some effects from the Pacific SST anomalies associated with the AMO changes. However, given the dipole SAT response to IPO in the Arctic and the orthogonality between the PC1 and PC2, the contribution from IPO in our estimated AMO's impact is likely small. Nevertheless, more studies are needed on the relationship between the North Atlantic and tropical Pacific and its impact on the Arctic.

The last cold phase of the AMO occurred over 20 years ago in the 1990s; emerging evidence indicates that the North Atlantic subpolar gyre is already cold and is probably developing into a cold AMO (Frajka-Williams et al., 2017). If this occurs, Arctic warming trend is likely to slow down in the next few decades, but cooling like in the mid-20th century is unlikely to happen as the externally forced warming trend is much stronger after the 1980s. Furthermore, recent studies suggest that nonlinear responses to external forcings are more pronounced in the Arctic than at lower latitudes (Deng et al., 2020; Pauling et al., 2021), which requires further investigation since external forcing plays a major role in determining the overall warming rate of the future Arctic.

Data Availability Statement

This article is based entirely on public data sets. The BEST, GISTEMP4, HadCRUT5 observational data was provided by Rohde et al. (2013), Lenssen et al. (2019), and Morice et al. (2020), respectively. The ERA5 and ERA20C reanalysis data sets are from Hersbach et al. (2020) and Poli et al. (2016). CESM2LE, CESM1LE, and CMIP6 simulations are introduced by Rodgers et al. (2021), Kay et al. (2015), and Eyring et al. (2016). CESM2 single-forcing, CESM2-CMIP5 forcing, and CESM1 idealized pacemaker simulations are downloaded through the NCAR Climate Data Gateway (https://www.earthsystemgrid.org/dataset/ucar.cgd.cesm2.cmip5.forcing.html, https://www.earthsystemgrid.org/dataset/ucar.cgd.cesm2.single.forcing.large.ensemble.html, https://www.earthsystemgrid.org/dataset/ucar.cgd.ccsm4.IPO-PACEMAKER.html, and https://www.earthsystemgrid.org/dataset/ucar.cgd.ccsm4.amv_lens.html).

Acknowledgments
X. Chen was supported by the National Natural Science Foundation of China (2022YFF0801701, 42105017) and China Postdoctoral Science Foundation (BX20200087). A. Dai was supported by the National Science Foundation (Grants AGS-2015780 and OISE-1743738).

References

Auclair, G., & Tremblay, L. B. (2018). The role of ocean heat transport in rapid sea ice declines in the community Earth system model large ensemble. *Journal of Geophysical Research: Oceans*, *123*(12), 8941–8957. https://doi.org/10.1029/2018jc014525

Baxter, I., Ding, Q., Schweiger, A., L'Heureux, M., Baxter, S., Wang, T., et al. (2019). How tropical Pacific surface cooling contributed to accelerated sea ice melt from 2007 to 2012 as ice is thinned by anthropogenic forcing. *Journal of Climate*, *32*(24), 8583–8602. https://doi.org/10.1175/jcli-d-18-0783.1

Beitsch, A., Jungclaus, J. H., & Zanchettin, D. (2014). Patterns of decadal-scale Arctic warming events in simulated climate. *Climate Dynamics*, *43*(7–8), 1773–1789. https://doi.org/10.1007/s00382-013-2004-5

Bengtsson, L., Semenov, V. A., & Johannessen, O. M. (2004). The early twentieth-century warming in the Arctic—A possible mechanism. *Journal of Climate*, *17*(20), 4045–4057. https://doi.org/10.1175/1520-0442(2004)017<4045:tetwit>2.0.co;2

Bokuchava, D. D., & Semenov, V. A. (2021). Mechanisms of the early 20th century warming in the Arctic. *Earth-Science Reviews*, *222*, 103820. https://doi.org/10.1016/j.earscirev.2021.103820

Booth, B. B. B., Dunstone, N. J., Halloran, P. R., Andrews, T., & Bellouin, N. (2012). Aerosols implicated as a prime driver of twentieth-century North Atlantic climate variability. *Nature*, *484*(7393), 228–232. https://doi.org/10.1038/nature10946

Cai, Q., Wang, J., Beletsky, D., Overland, J., Ikeda, M., & Wan, L. (2021). Accelerated decline of summer Arctic sea ice during 1850–2017 and the amplified Arctic warming during the recent decades. *Environmental Research Letters*, *16*(3), 034015. https://doi.org/10.1088/1748-9326/abdb5f

Cai, W., Wu, L., Lengaigne, M., Li, T., McGregor, S., Kug, J.-S., et al. (2019). Pantropical climate interactions. *Science*, *363*(6430), eaav4236. https://doi.org/10.1126/science.aav4236

Castruccio, F. S., Ruprich-Robert, Y., Yeager, S. G., Danabasoglu, G., Msadek, R., & Delworth, T. L. (2019). Modulation of Arctic sea ice loss by atmospheric teleconnections from Atlantic multidecadal variability. *Journal of Climate*, *32*(5), 1419–1441. https://doi.org/10.1175/jcli-d-18-0307.1

Chen, X., Luo, D., Feldstein, S. B., & Lee, S. (2018). Impact of winter Ural blocking on Arctic sea ice: Short-time variability. *Journal of Climate*, *31*(6), 2267–2282. https://doi.org/10.1175/jcli-d-17-0194.1

Chylek, P., Folland, C., Klett, J. D., Lesins, G., & Dubey, M. K. (2023). Arctic amplification in the community Earth system models (CESM1 and CESM2). *Atmosphere*, *14*(5), 820. https://doi.org/10.3390/atmos14050820

Chylek, P., Folland, C. K., Lesins, G., Dubey, M. K., & Wang, M. (2009). Arctic air temperature change amplification and the Atlantic multidecadal oscillation. *Geophysical Research Letters*, *36*(14), L14801. https://doi.org/10.1029/2009gl038777

Chylek, P., Hengartner, N., Lesins, G., Klett, J. D., Humlum, O., Wyatt, M., & Dubey, M. K. (2014). Isolating the anthropogenic component of Arctic warming. *Geophysical Research Letters*, *41*(10), 3569–3576. https://doi.org/10.1002/2014gl060184

Clark, J. P., & Lee, S. (2019). The role of the tropically excited Arctic warming mechanism on the warm Arctic cold continent surface air temperature trend pattern. *Geophysical Research Letters*, *46*(14), 8490–8499. https://doi.org/10.1029/2019gl082714

Dai, A., & Deng, J. (2022). Recent Eurasian winter cooling partly caused by internal multidecadal variability amplified by Arctic sea ice-air interactions. *Climate Dynamics*, *58*(11–12), 1–17. https://doi.org/10.1007/s00382-021-06095-y

Dai, A., Fyfe, J. C., Xie, S.-P., & Dai, X. (2015). Decadal modulation of global surface temperature by internal climate variability. *Nature Climate Change*, *5*(6), 555–559. https://doi.org/10.1038/nclimate2605

Dai, A., Luo, D., Song, M., & Liu, J. (2019). Arctic amplification is caused by sea-ice loss under increasing CO_2. *Nature Communications*, *10*, 1–13. https://doi.org/10.1038/s41467-018-07954-9

Danabasoglu, G., Lamarque, J. F., Bacmeister, J., Bailey, D., DuVivier, A., Edwards, J., et al. (2020). The community Earth system model version 2 (CESM2). *Journal of Advances in Modeling Earth Systems*, *12*, e2019MS001916. https://doi.org/10.1029/2019ms001916

Davy, R., & Outten, S. (2020). The Arctic surface climate in CMIP6: Status and developments since CMIP5. *Journal of Climate*, *33*(18), 8047–8068. https://doi.org/10.1175/jcli-d-19-0990.1

Deng, J., & Dai, A. (2022). Sea ice–air interactions amplify multidecadal variability in the North Atlantic and Arctic region. *Nature Communications*, *13*, 1–13. https://doi.org/10.1038/s41467-022-29810-7

Deng, J., Dai, A., & Xu, H. (2020). Nonlinear climate responses to increasing CO_2 and anthropogenic aerosols simulated by CESM1. *Journal of Climate*, *33*(1), 281–301. https://doi.org/10.1175/jcli-d-19-0195.1

Deser, C., & Phillips, A. S. (2009). Atmospheric circulation trends, 1950–2000: The relative roles of sea surface temperature forcing and direct atmospheric radiative forcing. *Journal of Climate*, *22*(2), 396–413. https://doi.org/10.1175/2008jcli2453.1

Ding, Q., Schweiger, A., L'Heureux, M., Battisti, D. S., Po-Chedley, S., Johnson, N. C., et al. (2017). Influence of high-latitude atmospheric circulation changes on summertime Arctic sea ice. *Nature Climate Change*, *7*(4), 289–295. https://doi.org/10.1038/nclimate3241

Ding, Q., Schweiger, A., L'Heureux, M., Steig, E. J., Battisti, D. S., Johnson, N. C., et al. (2019). Fingerprints of internal drivers of Arctic sea ice loss in observations and model simulations. *Nature Geoscience*, *12*(1), 28–33. https://doi.org/10.1038/s41561-018-0256-8

Ding, Q., Wallace, J. M., Battisti, D. S., Steig, E. J., Gallant, A. J., Kim, H.-J., & Geng, L. (2014). Tropical forcing of the recent rapid Arctic warming in northeastern Canada and Greenland. *Nature*, *509*(7499), 209–212. https://doi.org/10.1038/nature13260

England, M. R. (2021). Are multi-decadal fluctuations in Arctic and Antarctic surface temperatures a forced response to anthropogenic emissions or part of internal climate variability? *Geophysical Research Letters*, *48*(6), e2020GL090631. https://doi.org/10.1029/2020gl090631

England, M. R., Eisenman, I., Lutsko, N. J., & Wagner, T. J. (2021). The recent emergence of Arctic amplification. *Geophysical Research Letters*, *48*(15), e2021GL094086. https://doi.org/10.1029/2021gl094086

Eyring, V., Bony, S., Meehl, G. A., Senior, C. A., Stevens, B., Stouffer, R. J., & Taylor, K. E. (2016). Overview of the coupled model intercomparison project phase 6 (CMIP6) experimental design and organization [Dataset]. *Geoscientific Model Development*, *9*(5), 1937–1958. https://doi.org/10.5194/gmd-9-1937-2016

Frajka-Williams, E., Beaulieu, C., & Duchez, A. (2017). Emerging negative Atlantic multidecadal oscillation index in spite of warm subtropics. *Scientific Reports*, *7*(1), 11224. https://doi.org/10.1038/s41598-017-11046-x

Francis, J. A., & Wu, B. (2020). Why has no new record-minimum Arctic sea-ice extent occurred since September 2012? *Environmental Research Letters*, *15*(11), 114034. https://doi.org/10.1088/1748-9326/abc047

Fyfe, J. C., Kharin, V. V., Santer, B. D., Cole, J. N., & Gillett, N. P. (2021). Significant impact of forcing uncertainty in a large ensemble of climate model simulations. *Proceedings of the National Academy of Sciences of the United States of America*, *118*(23), e2016549118. https://doi.org/10.1073/pnas.2016549118

Fyfe, J. C., von Salzen, K., Gillett, N. P., Arora, V. K., Flato, G. M., & McConnell, J. R. (2013). One hundred years of Arctic surface temperature variation due to anthropogenic influence. *Scientific Reports*, *3*, 1–7. https://doi.org/10.1038/srep02645

Goosse, H., & Holland, M. M. (2005). Mechanisms of decadal Arctic climate variability in the community climate system model, version 2 (CCSM2). *Journal of Climate*, *18*(17), 3552–3570. https://doi.org/10.1175/jcli3476.1

Henley, B. J., Gergis, J., Karoly, D. J., Power, S., Kennedy, J., & Folland, C. K. (2015). A tripole index for the interdecadal Pacific oscillation. *Climate Dynamics*, *45*(11–12), 3077–3090. https://doi.org/10.1007/s00382-015-2525-1

Hersbach, H., Bell, B., Berrisford, P., Hirahara, S., Horányi, A., Muñoz-Sabater, J., et al. (2020). The ERA5 global reanalysis [Dataset]. *Quarterly Journal of the Royal Meteorological Society*, *146*(730), 1999–2049. https://doi.org/10.1002/qj.3803

Hua, W., Dai, A., & Qin, M. (2018). Contributions of internal variability and external forcing to the recent Pacific decadal variations. *Geophysical Research Letters*, *45*(14), 7084–7092. https://doi.org/10.1029/2018gl079033

Hurrell, J. W., Holland, M. M., Gent, P. R., Ghan, S., Kay, J. E., Kushner, P. J., et al. (2013). The community Earth system model: A framework for collaborative research. *Bulletin of the American Meteorological Society*, *94*(9), 1339–1360. https://doi.org/10.1175/bams-d-12-00121.1

Jenkins, M. T., & Dai, A. (2022). Arctic climate feedbacks in ERA5 reanalysis: Seasonal and spatial variations and the impact of sea-ice loss. *Geophysical Research Letters*, *49*(16), e2022GL099263. https://doi.org/10.1029/2022gl099263

Johannessen, O. M., Bengtsson, L., Miles, M. W., Kuzmina, S. I., Semenov, V. A., Alekseev, G. V., et al. (2004). Arctic climate change: Observed and modelled temperature and sea-ice variability. *Tellus A: Dynamic Meteorology and Oceanography*, *56*(5), 328–341. https://doi.org/10.3402/tellusa.v56i5.14599

Jungclaus, J. H., & Koenigk, T. (2010). Low-frequency variability of the Arctic climate: The role of oceanic and atmospheric heat transport variations. *Climate Dynamics*, *34*(2–3), 265–279. https://doi.org/10.1007/s00382-009-0569-9

Kay, J. E., Deser, C., Phillips, A., Mai, A., Hannay, C., Strand, G., et al. (2015). The community Earth system model (CESM) large ensemble Project: A community resource for studying climate change in the presence of internal climate variability [Dataset]. *Bulletin of the American Meteorological Society*, *96*(8), 1333–1349. https://doi.org/10.1175/bams-d-13-00255.1

Kwok, R., Spreen, G., & Pang, S. (2013). Arctic sea ice circulation and drift speed: Decadal trends and ocean currents. *Journal of Geophysical Research: Oceans*, *118*(5), 2408–2425. https://doi.org/10.1002/jgrc.20191

Lenssen, N. J., Schmidt, G. A., Hansen, J. E., Menne, M. J., Persin, A., Ruedy, R., & Zyss, D. (2019). Improvements in the GISTEMP uncertainty model [Dataset]. *Journal of Geophysical Research: Atmospheres*, *124*(12), 6307–6326. https://doi.org/10.1029/2018jd029522

Li, X., Xie, S.-P., Gille, S. T., & Yoo, C. (2016). Atlantic-induced pan-tropical climate change over the past three decades. *Nature Climate Change*, *6*(3), 275–279. https://doi.org/10.1038/nclimate2840

Liu, Z., Risi, C., Codron, F., He, X., Poulsen, C. J., Wei, Z., et al. (2021). Acceleration of western Arctic sea ice loss linked to the Pacific North American pattern. *Nature Communications*, *12*, 1–9. https://doi.org/10.1038/s41467-021-21830-z

Mann, M. E., & Emanuel, K. A. (2006). Atlantic hurricane trends linked to climate change. *Eos, Transactions American Geophysical Union*, *87*(24), 233–241. https://doi.org/10.1029/2006eo240001

McGregor, S., Timmermann, A., Stuecker, M. F., England, M. H., Merrifield, M., Jin, F.-F., & Chikamoto, Y. (2014). Recent Walker circulation strengthening and Pacific cooling amplified by Atlantic warming. *Nature Climate Change*, *4*(10), 888–892. https://doi.org/10.1038/nclimate2330

Meehl, G. A., Arblaster, J. M., Bates, S., Richter, J. H., Tebaldi, C., Gettelman, A., et al. (2020). Characteristics of future warmer base states in CESM2. *Earth and Space Science*, *7*(9), e2020EA001296. https://doi.org/10.1029/2020ea001296

Meehl, G. A., Hu, A., Castruccio, F., England, M. H., Bates, S. C., Danabasoglu, G., et al. (2021). Atlantic and Pacific tropics connected by mutually interactive decadal-timescale processes. *Nature Geoscience*, *14*(1), 36–42. https://doi.org/10.1038/s41561-020-00669-x

Morice, C. P., Kennedy, J. J., Rayner, N. A., Winn, J. P., Hogan, E., Killick, R. E., et al. (2020). An updated assessment of near-surface temperature change from 1850: The Had-CRUT5 dataset [Dataset]. *Journal of Geophysical Research: Atmospheres*, *126*, e2019JD032361. https://doi.org/10.1029/2019JD032361

Murphy, L. N., Bellomo, K., Cane, M., & Clement, A. (2017). The role of historical forcings in simulating the observed Atlantic multidecadal oscillation. *Geophysical Research Letters*, *44*(5), 2472–2480. https://doi.org/10.1002/2016gl071337

Nozawa, T., Nagashima, T., Shiogama, H., & Crooks, S. A. (2005). Detecting natural influence on surface air temperature change in the early twentieth century. *Geophysical Research Letters*, *32*(20), L20719. https://doi.org/10.1029/2005GL023540

Okumura, Y., Xie, S.-P., Numaguti, A., & Tanimoto, Y. (2001). Tropical Atlantic air-sea interaction and its influence on the NAO. *Geophysical Research Letters*, *28*(8), 1507–1510. https://doi.org/10.1029/2000gl012565

Pauling, A. G., Bushuk, M., & Bitz, C. M. (2021). Robust inter-hemispheric asymmetry in the response to symmetric volcanic forcing in model large ensembles. *Geophysical Research Letters*, *48*(9), e2021GL092558. https://doi.org/10.1029/2021gl092558

Peings, Y., & Magnusdottir, G. (2016). Wintertime atmospheric response to Atlantic multidecadal variability: Effect of stratospheric representation and ocean–atmosphere coupling. *Climate Dynamics*, *47*(3–4), 1029–1047. https://doi.org/10.1007/s00382-015-2887-4

Poli, P., Hersbach, H., Dee, D. P., Berrisford, P., Simmons, A. J., Vitart, F., et al. (2016). ERA-20C: An atmospheric reanalysis of the twentieth century [Dataset]. *Journal of Climate*, *29*(11), 4083–4097. https://doi.org/10.1175/jcli-d-15-0556.1

Polyakov, I. V., & Johnson, M. A. (2000). Arctic decadal and interdecadal variability. *Geophysical Research Letters*, *27*(24), 4097–4100. https://doi.org/10.1029/2000gl011909

Qin, M., Dai, A., & Hua, W. (2020a). Quantifying contributions of internal variability and external forcing to Atlantic multidecadal variability since 1870. *Geophysical Research Letters*, *47*(22), e2020GL089504. https://doi.org/10.1029/2020gl089504

Qin, M., Dai, A., & Hua, W. (2020b). Aerosol-forced multidecadal variations across all ocean basins in models and observations since 1920. *Science Advances*, *6*(29), eabb0425. https://doi.org/10.1126/sciadv.abb0425

Rayner, N., Parker, D. E., Horton, E., Folland, C. K., Alexander, L. V., Rowell, D., et al. (2003). Global analyses of sea surface temperature, sea ice, and night marine air temperature since the late nineteenth century. *Journal of Geophysical Research*, *108*(D14), 4407. https://doi.org/10.1029/2002jd002670

Rodgers, K. B., Lee, S.-S., Rosenbloom, N., Timmermann, A., Danabasoglu, G., Deser, C., et al. (2021). Ubiquity of human-induced changes in climate variability [Dataset]. *Earth System Dynamics*, *12*(4), 1393–1411. https://doi.org/10.5194/esd-12-1393-2021

Rohde, R., Muller, R., Jacobsen, R., Muller, E., Perlmutter, S., Rosenfeld, A., et al. (2013). A new estimate of the average Earth surface land temperature spanning 1753 to 2011 [Dataset]. *Geoinfor Geostat: An overview 1:1*, *7*. https://berkeley-earth-temperature.s3.us-west-1.amazonaws.com/Global/Gridded/Land_and_Ocean_LatLong1.nc

Sang, X., Yang, X.-Q., Tao, L., Fang, J., & Sun, X. (2021). Decadal changes of wintertime poleward heat and moisture transport associated with the amplified Arctic warming. *Climate Dynamics*, *58*(1–2), 1–23. https://doi.org/10.1007/s00382-021-05894-7

Serreze, M. C., & Barry, R. G. (2011). Processes and impacts of Arctic amplification: A research synthesis. *Global and Planetary Change*, *77*(1–2), 85–96. https://doi.org/10.1016/j.gloplacha.2011.03.004

Serreze, M. C., & Francis, J. A. (2006). The Arctic amplification debate. *Climatic Change*, *76*(3–4), 241–264. https://doi.org/10.1007/s10584-005-9017-y

Simpson, I. R., Bacmeister, J., Neale, R. B., Hannay, C., Gettelman, A., Garcia, R. R., et al. (2020). An evaluation of the large-scale atmospheric circulation and its variability in CESM2 and other CMIP models. *Journal of Geophysical Research: Atmospheres*, *125*(13), e2020JD032835. https://doi.org/10.1029/2020jd032835

Sorteberg, A., & Kvingedal, B. (2006). Atmospheric forcing on the Barents Sea winter ice extent. *Journal of Climate*, *19*, 4772–4784. https://doi.org/10.1175/jcli3885.1

Sun, C., Kucharski, F., Li, J., Wang, K., Kang, I. S., Lian, T., et al. (2019). Spring Aleutian low weakening and surface cooling trend in northwest North America during recent decades. *Journal of Geophysical Research: Atmospheres*, *124*(22), 12078–12092. https://doi.org/10.1029/2019jd031405

Suo, L., Otterå, O. H., Bentsen, M., Gao, Y., & Johannessen, O. M. (2013). External forcing of the early 20th century Arctic warming. *Tellus A: Dynamic Meteorology and Oceanography*, *65*(1), 20578. https://doi.org/10.3402/tellusa.v65i0.20578

Svendsen, L., Keenlyside, N., Bethke, I., Gao, Y., & Omrani, N.-E. (2018). Pacific contribution to the early twentieth-century warming in the Arctic. *Nature Climate Change*, *8*(9), 793–797. https://doi.org/10.1038/s41558-018-0247-1

Svendsen, L., Keenlyside, N., Muilwijk, M., Bethke, I., Omrani, N.-E., & Gao, Y. (2021). Pacific contribution to decadal surface temperature trends in the Arctic during the twentieth century. *Climate Dynamics*, *57*(11–12), 3223–3243. https://doi.org/10.1007/s00382-021-05868-9

Ting, M., Kushnir, Y., Seager, R., & Li, C. (2009). Forced and internal twentieth-century SST trends in the North Atlantic. *Journal of Climate*, *22*(6), 1469–1481. https://doi.org/10.1175/2008jcli2561.1

Tokinaga, H., Xie, S.-P., & Mukougawa, H. (2017). Early 20th-century Arctic warming intensified by Pacific and Atlantic multidecadal variability. *Proceedings of the National Academy of Sciences of the United States of America*, *114*(24), 6227–6232. https://doi.org/10.1073/pnas.1615880114

Wang, S., & Chen, W. (2021). Impact of internal variability on recent opposite trends in wintertime temperature over the Barents–Kara Seas and central Eurasia. *Climate Dynamics*, *58*(11–12), 1–16. https://doi.org/10.1007/s00382-021-06077-0

Watanabe, M., & Tatebe, H. (2019). Reconciling roles of sulphate aerosol forcing and internal variability in Atlantic multidecadal climate changes. *Climate Dynamics*, *53*(7–8), 4651–4665. https://doi.org/10.1007/s00382-019-04811-3

Ye, K., & Messori, G. (2021). Inter-model spread in the wintertime Arctic amplification in the CMIP6 models and the important role of internal climate variability. *Global and Planetary Change*, *204*, 103543. https://doi.org/10.1016/j.gloplacha.2021.103543

Zhang, R. (2015). Mechanisms for low-frequency variability of summer Arctic sea ice extent. *Proceedings of the National Academy of Sciences of the United States of America*, *112*(15), 4570–4575. https://doi.org/10.1073/pnas.1422296112

Zhang, X., Sorteberg, A., Zhang, J., Gerdes, R., & Comiso, J. C. (2008). Recent radical shifts of atmospheric circulations and rapid changes in Arctic climate system. *Geophysical Research Letters*, *35*(22), L22701. https://doi.org/10.1029/2008gl035607